Active microrheology with a single, time-shared laser trap

Frederic Català-Castro[1]*, Santiago Ortiz-Vásquez[1]*, Carmen Martínez-Fernández[1]*, Fabio Pezzano[2], Carla Garcia-Cabau[3], Senda Jiménez-Delgado[2], Xavier Salvatella[3,4], Verena Ruprecht[2,4,5], Paolo-Antonio Frigeri[6,7], Michael Krieg[1,7]

(1) ICFO - Institut de Ciències Fotòniques, Castelldefels, The Barcelona Institute of Science and Technology, Barcelona, Spain;
(2) Center for Genomic Regulation (CRG), The Barcelona Institute of Science and Technology, Barcelona, Spain.
(3) Institute for Research in Biomedicine (IRB Barcelona), The Barcelona Institute of Science and Technology, Barcelona, Spain
(4) ICREA, Pg. Lluis Companys 23, Barcelona 08010, Spain.
(5) Universitat Pompeu Fabra (UPF), Barcelona, Spain
(6) Impetux Optics, Spain
(7) correspondonce to: pafrigeri@gmail.com, michael.krieg@icfo.eu

Abstract

Recording the mechanical response of biological samples, the cell's interior and complex fluids in general, would enable deeper understanding of cellular differentiation, ageing and drug discovery. Here, we present a time-shared optical tweezer microrheology (TimSOM) pipeline to determine the frequency- and age-dependent viscoelastic properties of biological materials. Our approach consists in splitting a single laser beam into two near-instantaneous time-shared optical traps to carry out simultaneous force and displacement measurements with sub-nanometer and sub-picoNewton accuracy during sinusoidal perturbations. Leveraging numerical and analytical models, we find solutions to commonly encountered deviations, to build an artefact-free nanorheometer. We demonstrate the versatility of the technique by 1) measuring the phase transitions of an ageing biomolecular condensate, 2) quantifying the complex viscoelastic properties of three intracellular compartments of zebrafish progenitor cells, and, using *Caenorhabditis elegans*, we uncover how mutations causing nuclear envelopathies soften the cytosol of intestinal cells during organismal age. Together, our advances afford rapid phenotyping of material properties inside cells and proteins blends, opening avenues for biomedical and drug screening applications.

Keywords

Optical tweezers, microrheology, cell biophysics, mechanobiology, cell nucleus, LLPS

1 Main

All fluids, cells and their organelles in a human body consist primarily of water, sugar and proteins. The many weak interactions between the individual components gives rise to complex/non-Newtonian fluids, which are characterized by a frequency-dependent, viscoelastic response to internal and external forces. How complex fluids deform and flow in relation to their chemical composition is the science of rheology[1]. The rheology of biological fluids is crucial for a variety of physiological and pathological processes[2, 3], including cell division[4], cell migration[5], mechanotransduction[6, 7, 8] and intracellular transport [9]. Recent data data indicates that alterations in the way cells and their components react to mechanical forces are linked to various diseases, such as cancer and neurodegeneration[3, 10, 11, 12]. In particular, many phase-separated, liquid-like condensates exhibit age-dependent mechanical properties[13, 14, 6]. Their transition from a liquid-like to a gel/glassy state has been associated with a poor prognosis of many neurodegenerative disorders[13]. Thus, the precise characterization of their time-dependent microrheological properties could obtain valuable insights for drug-development and diagnosis.

Optical tweezer-based active microrheology is a powerful technique for probing the mechanical properties of complex fluids in biological systems, such as the cytoplasm of living cells [4, 15], in living animals [16, 17] and biomolecular condensates [14, 6, 18]. This method involves the measurement of the motion of small particles suspended within a fluid (or embedded in a viscoelastic gel), due to an oscillating trapping potential [19]. The resulting response function, defined in the frequency domain as $\hat{\chi}(\omega) = \hat{x}_p(\omega)/\hat{F}(\omega)$, which relates the probe displacement $\hat{x}_p(\omega)$ to the active force $\hat{F}(\omega)$, captures the frequency-dependent elasticity and viscosity of the material. Optical tweezers are particularly well suited to derive material properties of biological materials as they operate in the pN range characteristic for molecular interactions and can measure the position of micron-sized objects with sub-nanometer accuracy. Moreover, optical tweezers can trap small microspheres (with radius $r_{\mathrm{bead}} \approx 10^{-7}$m) making them particularly useful to measure their response to force embedded into very small volumes (e.g. $V_{\mathrm{cell}} = 10^{-15}$ vs. $V_{\mathrm{bead}} = 10^{-19}$ m^3), e.g. in living cells, purified protein blends or novel synthetic materials and therefore afford applications where samples are precious. The small scale of deformations

also permits the analysis of the heterogeneity of the response, rather than providing a bulk-modulus from macroscopic measurements, a key point for experiments targeting subcellular mechanical compartmentalization.

The widespread application of active microrheology with optical gradient forces, however, is practically limited by the complicated alignment of two laser beams that are required to simultaneously measure bead displacement and force during the measurement [20, 21, 16, 17, 4]. In this standard approach, the detection laser is static, while the trapping laser is oscillated at different frequencies. Alternatively, a single laser can be split into two beams with orthogonal polarization [22]. Likewise, it does, however, suffer from the drawback of having to align two different optical paths and having to introduce two pairs of deflectors and detectors as in the case of using a separate detection laser (Fig. 1a).

In this article, we present an active microrheology method with a single time-shared laser generating two distinct optical traps - one that drives the active oscillation, while the second one acts as a static, displacement detection beam (Fig. 1b). We first theoretically established that a fast, 25 kHz beam sharing generates a quasi continuous trapping potentials for simultaneous force and displacement measurements. In combination with direct, momentum-based force measurement, this method productively simplifies the rheology routines, without tedious calibrations and alignments of multiple lasers prior to measurements inside cell and animals, or complex fluids. Because the two traps appear intermittently and complementary to each other, we introduce corrections to compensate for the deviation of the raw measurements obtained by time-sharing compared to the expected result for two simultaneous traps.

To demonstrate the versatility of the time-shared optical tweezer microrheology (TimSOM), we measured the rheological spectrum over frequencies ranging from 0.5 Hz to $2 \cdot 10^3$ Hz on biomolecular condensates, in the cytoplasm, cytoplasm/nucleus interfase and nucleoplasm of progenitor cells isolated from zebrafish embryos, and quantified how the complex shear modulus of *Caenorhabditis elegans* changes during age.

2 Results

2.1 Theory and experimental implementation of time-shared optical microrheology

The measurement of the mechanical and rheological properties requires the simultaneous recording of stress and strain. Using optical tweezers, this is equivalent to measuring the optical force acting onto an optically-trapped probe and the displacement resulting from such force. A direct force sensor is commonly used to measure the force through the change in the trapping beam light momentum tracked at the back focal plane (BFP) [23, 24, 25, 26] (Fig. 1a). Simultaneously, probe displacements are commonly obtained through BFP interferometry after calibration of the sensitivity factor, β (µm/V) [27], of an additional position-sensitive detector capturing a detection laser interfering with the trapped probe. Together, these provide picoNewton and nanometer sensitivity.

To conceptualize a simplified microrheology experiment, we consider a *single* laser that creates two traps with identical power, position sensitivity $\beta_1 = \beta_2 \equiv \beta$ and trapping stiffness $k_1 = k_2 \equiv k/2$, where k is the sum of the stiffness of the two traps (Fig. 1b). At the beginning of the experiment, both traps are centered on the microsphere. Trap 1, the so-called *driving trap*, starts to oscillate at a given frequency ω, i.e. $x_1(t) = 2x\sin(\omega t)$, while trap 2, the so-called *detection trap*, remains fixed at $x_2(t) = 0$ (Figure 1b). Because the displacement of the driving trap is in the linear regime, contributions of the force from the driving and detection traps need to be taken into account such that the particle will feel a total force of $F_T(t) = F_1(t) + F_2(t)$. At a given stimulation frequency (ω), the response of the particle position $\hat{\chi}(\omega)$ as it enters from the passive position to the new position can be described with the complex response function $\hat{\chi}(\omega)$ and the complex G modulus $\hat{G}(\omega)$ (see Suppl. Text for the derivation):

$$\hat{\chi}(\omega) = \frac{\hat{x}(\omega)}{\hat{F}_{tot}(\omega)} = -\frac{2\hat{V}_2(\omega)}{k\left[\hat{V}_1(\omega) + \hat{V}_2(\omega)\right]} \tag{1a}$$

$$\hat{G}(\omega) = \frac{1}{6\pi a} \cdot \frac{1}{\hat{\chi}(\omega)} = -\frac{k}{12\pi a} \cdot \frac{\hat{V}_1(\omega) + \hat{V}_2(\omega)}{\hat{V}_2(\omega)} \tag{1b}$$

Interestingly, due to the symmetry between the two traps, equations 1 do not depend on the displacement sensitivity β (µm/V). Thus, the accuracy of our method strictly depends on the ability to generate

two identical traps with the same stiffness, k (pN/V), from a single laser source, as well as the bandwidth of the measurement of the relative voltage change (see Supplementary Text). This is straightforward in a set-up modulated with fast-scanning acusto-optic deflectors (AODs) [28, 29] and equipped with direct light momentum force detection [23]. In such configuration (Fig. 2a), the laser spot is alternating between traps 1 and 2 at the time-sharing frequency, f_{TS}. This has usually been considered fast enough compared to the trapped particle diffusion dynamics, hence creating a stable optical trap with an average trapping power [30, 31, 32]. The stiffness of the trap now is the single most important parameter which sets the limits of the experimentally accessible material properties. It can be shown that time-sharing rheology works best when the absolute value of the complex shear modulus $G(\omega)$ is much higher than the strength of the trap ($G_0 = \frac{k}{12\pi a}$) (Supplementary Text). In that case, the voltage change of the active trap dramatically surpasses the passive voltage change ($|V_1(t) + V_2(t)| >> |V_2(t)|$). However, in cases where the strength of the trap surpasses the complex G modulus of the sample, the bead jumps instantaneously between the two traps without deflection such that $V_1 \approx V_2$. This can be explained by the fact that the traps alternate between $x_1(t)$ and $x_2(t)$. This creates a deviation from the expected viscoelastic behaviour in the high frequency range beyond the cross-over frequency, where the elastic contributions dominate.

To understand and eventually correct for this deviation, we modeled the displacement of the particle under the influence of the two intermittent traps and analyzed the subsequent artifacts introduced into $\hat{\chi}_t(\omega)$ (Fig. 2b). As a generalization of nanometer-scale microrheology, we considered that the probe microspheres are embedded in a viscoelastic matrix that is best described by power laws [33], in particular, by the Kelvin-Voigt or Maxwell fractional models [34]. These are generalized viscoelastic models that extend the applicability of the classical Kelvin-Voigt, Maxwell and structural damping models, to describe with few parameters the power-law behaviour of most biological samples and gels (see [34] and Supplementary Text). We addressed the analysis of the artifacts through two approaches that are described in detail in the Supplementary Text. First, we solved the probe trajectory using the fractional derivative equations (FDE) that describe motion in materials with power law rheology (Fig. 2d). Second, we obtained an analytical solution of the probe motion —and the resulting $\hat{\chi}_t(\omega)$— through a first

harmonic approximation of the trap positioning sequence in the frequency domain. As demonstrated in Fig. 2d, the artifact-free response function is retrieved successfully after the compensation.

We then compared the response function of the time-shared method with the ideal, time-continuous response function after solving the equation of motion of the particle in the frequency domain numerically and analytically (Fig. 2c,d). We confidently conclude that time-sharing measurements correctly reflect the behaviour for viscoelastic solids, e.g. Kelvin-Voigt materials — up to 2000 Hz, deviations from ideal behaviour a less than 15% and with our compensation routines (see Supplementary Text), the residual deviation can efficiently be compensated. For viscoelastic liquids, e.g. Maxwell materials, the deviations strongly affect the real part of the response function, such that the fractional solid behaviour at frequencies larger than the crossover frequency is not accessed for inadequately stiff traps. Our simulations also show that the imaginary part $\chi_1''(\omega)$ expresses the contribution resulting from the mixing between the real and imaginary parts of the response function, and that such mixing is proportional to the rigidity of the trap k. Thus, measuring the response function with different trap stiffness is able to break the degeneracy of the time-sharing technique and allows access to E in the Maxwell regime (for details on the compensation procedure see Supplementary Text).

In the particular case of an ideal and homogeneous Maxwell material, the time-sharing measurement degenerates and the elastic component of the material becomes inaccessible to the measurement if the trap stiffness is larger than $6\pi a\mu\omega$. We have developed a method to correct deviations caused by intermittent traps for various types of samples, including fractional Maxwell materials, as demonstrated in our theoretical and experimental findings (Supplementary Text). With this formalism in hand, we are now equipped to estimate the complex mechanics of most common biological material behaviour.

2.2 TimSOM measures 1 Pa-100 kPa over five decades of frequencies

Our theoretical analyses predicted that time-shared optical rheology demonstrates exceptional performance in viscoelastic materials. In order to experimentally validate the TimSOM scheme, we used three different materials with known rheological properties to extract the shear modulus through TimSOM over a frequency range from 2 Hz to 6.25 kHz. The viscosity of water (Supp. Data Fig. 2a) and the

different glycerol mixtures extracted from the time shared rheology were consistent with the values extracted from drag force measurements of a microsphere driven at different velocities (Supp. Data Fig. 2a iii). As expected for a purely viscous material, the storage modulus of water and glycerol at all concentrations was ill-defined over the whole frequency range (Supp. Data Fig. 2b). We then fabricated polyacrylamide (PA) gels with a very low degree of crosslinks (see Methods, E≈5-100 Pa). However, even though the bead returned to the equilibrium position by the polymer network restoring forces after a 20 µm displacement, we did not recover a purely elastic response (Supp. Data Fig. 2c). These soft gels were primarily viscoelastic and fit well to a fractional Kelvin-Voigt model. To confirm these results, we extracted the complex shear modulus from creep compliance measurements [35], $J(t)$, which are in close agreement to the TimSOM measurements (Supp. Data Fig. 2d).

Lastly, we also tested TimSOM on microspheres embedded in freshly prepared and uncured 10:0.1 PDMS prepolymer/curing agent mixtures (Supp. Data Fig. 2e). Consistent with previous reports, the pre-gelation PDMS was best described as a fractional Maxwell viscoelastic gel[34] with a plateau modulus at high frequencies of 0.1 MPa[36, 17]. This corresponded to a minimal displacement of the microsphere of less than 1 nm. Taken together, time-shared active microrheology is suitable to investigate the storage and loss moduli of viscous and viscoelastic materials with different properties, and retrieves viscoelastic moduli over five orders of magnitude over a five decade frequency range.

2.3 Deciphering the viscoelastic properties of ageing Maxwell liquids

To evaluate the capabilities of TimSOM to accelerate scientific discoveries with potential use for drug screening applications, we used TimSOM to measure the frequency-dependent mechanical properties of viscoelastic liquids and solids. Liquid-liquid phase separation is relevant for the organization of many proteins within the cytoplasm of living cells[37, 38]. The correct localization and material properties of these biomolecular condensates is essential for proper cellular functions[6] and is thus under tight cellular control [39] and the uncontrolled transition of liquid-like condensates into insoluble and stiffened condensates often correlate with disease propagation where a higher degree of stiffening correlates with disease prognosis.

Recently, laser tweezer rheology revealed that many biomolecular condensates behave as ageing Maxwell liquids, with an age-dependent change in viscosity[14]. These experiments are commonly performed in a dual optical trap, *dumbbell* configuration, in which a droplet is sandwiched between two trapped, active and passive microspheres (Fig. 3, [14, 40]). The complex shear modulus and surface tension of the material is then extracted from the active force measurement and passive bead displacement, with the assumption that the microsphere radius is considerably smaller than the protein droplet and that the viscosity of the dilute phase is known [41]. To relax these assumptions and simplify the experiment with a single trap, we performed TimSOM on MEC-2 condensates as a model for an age-dependent maturation process and compared these results to the dual trap assay[6] (Fig. 3). After applying the compensation routines for a fractional Maxwell material, we found a similar frequency response in both configurations that suggested a significant and noticeable shift in the cross-over frequency to lower values after 24 h of droplet formation (Fig. 3a, b). Interestingly, the values for stiffness and viscosity were slightly higher in the single bead assay, which measured the bulk modulus in the center of the droplet as opposed to the interfacial moduli. These differences suggest that the maturation process does not happen homogenous across the droplet instantaneously but affects center and periphery differently. Taken together, TimSOM accurately resolved the fractional Maxwell behaviour of ageing biomolecular condensates and uncovered a potential mechanism for the rigidity percolation transition across the condensate.

2.4 The nucleoplasm is a soft viscoelastic solid

Direct, momentum based optical force measurements have their greatest potential inside living cells, where traditional mechanics measurements are limited by laborious *in situ* calibrations[42, 19]. However, extracting information about their mechanics relies on the simultaneous measurement of deformation using a second detector (see above), in addition to the force. Thus, TimSOM should facilitate intracellular rheology without sacrificing simplicity and throughput. To demonstrate TimSOM inside cells, we performed active microrheology routines of three different compartments inside zebrafish germ layer progenitor cells. Following methods described previously[29], we introduced microspheres into

individual zebrafish embryos and extracted cells 4 hours-post-fertilization (hpf). We trapped individual microspheres to perform active microrheology routines in the cytoplasm and at the nuclear interface in the frequency range from 0.5 Hz-2 kHz using a 50-90 mW optical trap at the sample plane and calculated the complex shear modulus from the corresponding response function (see Supplementary Text). When performing the routines in the cytoplasm, we did not notice a significant history effect or non-linear mechanical response for the duration of the rheology routine, as we measured a constant phase lag between the trapping force and the probe oscillation throughout the measurement (Supp. Data Fig. 3). To compare the rheological properties between different cells and conditions, we used the fractional Kelvin-Voigt model which captures the frequency-dependent response of composite materials and parameterises the curves with 4 parameters ([4, 34], Supplementary Text 3). The frequency-dependent G modulus revealed a viscoelastic response with an elastic plateau at low frequencies (Fig. 4a) and a viscous response dominated at high frequencies. The cross-over frequency at which the dissipative forces dominate was $\approx$5 Hz and above, the cytoplasm fluidified as indicated by exponent β approaching 1 (Supp. Data Fig. 4b). Thus, the cytoplasmic rheology is consistent with a shear-thinning viscoelastic fluid, with a rubber-glass transition at high frequencies. This response was further shifted to lower frequencies after depolymerization of the dynamic actin cytoskeleton (Fig 4c and Supp. Data Fig. 4d), but not after disrupting myosin II motor activity (Supp. Data Fig. 5), indicating that the response in the cytoplasm is dominated by the actin network.

In general, we found that the cytoplasm was soft enough to re-position the same microsphere to the cytoplasmic/nuclear interface where we repeated the measurement with the aim to test the mechanical properties of the largest cellular organelle. In agreement with previous reports[43, 44], we found that the nuclear interface is stiffer than the cytoplasm (Fig. 4). To decipher which molecules determine the stiffness of the interface we tested cells overexpressing LaminA, major protein of the nuclear envelope, and disturbed actin networks. The shear modulus of the nuclear interface of LaminA expressing cells was indistinguishable from control cells which do not express high levels of LaminA endogenously[45, 46] even though the nuclear envelope was clearly stiffer as tested in a large-strain creep compliance test (Supp. Data Fig. 4e and 6). Actin around the nucleus was previously known to dampen and transmit

mechanical forces[47] and was observed in actin stainings of isolated gastrulating zebrafish progenitor cells (Supp. Data Fig. 7 and ref [48]). We thus speculated that actin has a noticeable effect on the mechanics of the nuclear interface. Indeed, after treating the cells with the actin depolymerizer Latrunculin A (LatA), cells immediately ceased blebbing and we already noticed a significant reduction in stiffness when we performed the large-strain creep-compliance test (Supp. Data Fig. 6). In our rheology experiment, we also found that the complex shear modulus of the nuclear interface was significantly reduced even though it remained significantly higher than the cytoplasm (Fig. 4, Supp. Data Fig. 4d) in absence of a functional actin network. Together, these data show that the rheology of the nuclear/cytoplasmic interface is stabilized by actin but unaffected by LaminA expression at the inner nuclear membrane.

To better understand the rheological properties of the nucleus itself, we mechanically inserted microspheres into the nucleoplasm (Supp. Data Fig. 6). Despite the relatively large shear moduli of the nuclear interface compared to the cytoplasm (Fig. 4a,b), the envelope was very flexible and deformed easily under modest forces exerted by the optical trap. When we applied a constant force of 100-150 pN onto the nuclear envelope, the microsphere entered into the nucleus which afforded the possibility to independently measure the rheology of the nucleoplasm (Fig. 4c, Supplementary Video 1). Importantly, the nuclei retained their integrity and functionality after microsphere insertion, as we did not observe leakage of DNA or soluble GFP (Supplementary Video 2) from the nucleus into the cytosol, and cell division proceeded indistinguishably from untreated cells with correct nuclear envelope breakdown and reassembly (Supplementary Video 3 and 4). Our rheology measurement of the nucleoplasm revealed a comparably soft material similar to the cytoplasm. The complex shear moduli, however, did not change in presence of LatA and the expression of LaminA (Supp. Data Fig. 4), indicating that the mechanical properties of the nucleoplasm is not dominated by the actin cytoskeleton and the nuclear envelope. Together, this indicates that with the same microsphere, we are able to measure the frequency dependent mechanical response of three cellular compartments and that the nucleoplasm is composed of a soft, viscoelastic material.

2.5 Premature ageing affects cytoplasmic viscoelasticity

Next, we applied TimSOM in specific tissues of *C. elegans*, a model system to understand the factors for organismal age. Ageing is a multifactorial process under genetic control[49], but how organismal age affects the mechanical properties of cells and tissues, however, is poorly understood. As a proof of principle, we specifically asked if the cytoplasm displays changes in rheological properties during the first eight days of age. Due to the difficulty in introducing microspheres into adult tissues without affecting animal physiology, we first established the use of endogenous lipid droplets as mechanical stress probes. Recent data demonstrates that cellular lipid droplets resist deformation when subjected to forces[50], cause itself nuclear indentations[50, 51] and activation of mechanotransduction pathways leading to hepatocyte differentiation[51]. Such droplets are abundant in various *C. elegans* tissues, including the intestinal epithelium (Fig. 5a) and the epidermis, where they were observed to mechanically rupture the nucleus without being deformed, and thus have a great potential to serve as endogenous force probes[52].

To establish these lipid droplets as *in vivo* force probes for rheology in *C. elegans*, we first confirmed that 1) their refractive index (n) is significantly higher than the surrounding cytoplasm (Fig. 5b), 2) they are ≈1µm in diameter to maximize trapping stiffness[53, 19] (Fig. 5c) and, 3) they are sufficiently stiff to be able to indent the desired target [50, 52]. We thus isolated lipid droplet from *C. elegans* using established procedures[54] and used iodixanol (idx) as index matching media [55] to determine their refractive index. At an idx concentration of 48%, the droplets where indistinguishable from the surrounding medium, which corresponds to n=1.42 (Fig. 5b). Thus, the lipid droplet's n was significantly larger than the cytoplasm(n=1.33-1.37, [56]). The diameter of the droplets was measured by scanning the optical trap across and applying a diameter look-up-table correction obtained from numerical simulations based on the T-matrix method [57] (Fig. 5c, Supp. Data Fig. 8). In order to confirm the suitability of lipid droplets as indenters, we first confirmed that they can be trapped and moved *in situ* and can cause a visible deformation of the nuclear envelope when they are moved against the nucleus with up to 200 pN of contact force (Fig. 5d). We next used purified droplets as rheological probes *in vitro* and embedded them into PA gels together with polystyrene microspheres as control probes. We then compared the

G modulus of the PA gel obtained through TimSOM with both probes. The G modulus of PA gels measured with lipid droplets coincided with that obtained from embedded polystyrene microspheres (Supp. Data Fig. 8). Together, this indicates that endogenous lipid droplets are sufficiently stiffer than other organelles, as also can be seen in their higher longitudinal modulus[58, 59], and are suitable as nano-indenters for optical force measurements.

We then trapped a single lipid droplet in the cytoplasm of intestinal epithelial cells and performed TimSOM from 0.5 Hz to 2 kHz. The rheological spectrum of day one adults fit well to a fractional Kelvin-Voigt model, indicative for the behaviour of a viscoelastic solid. Generally, the cytoplasm was 10 times stiffer than the cytoplasm of zebrafish progenitor cells (compare c_α, c_β; Fig. 4 with Supp. Data Fig. 9, and Fig. 5 with Supp. Data Fig. 4), which prevented us to probe multiple compartments with the same trapped object. This solid-like signature was slighty, but insignificantly reduced in day eight adults, suggesting a modest effect of age on viscoelastic properties of the cytoplasm (Fig. 5e). In attempt to define the genetic factors that contribute to cytoplasmic ageing, we performed TimSOM in mutants known to display premature ageing phenotypes in *C. elegans*. We tested a dominant negative *GFP::lmn-1*/LaminA construct, and mutations in *emr-1* Emerin and *lem-2* LEMD2 whose human homologs are implicated in muscle waste disorders and progerias[60, 61]. Many of these proteins localize to the inner nuclear membrane and are involved in coupling heterochromatin to the nuclear envelope. Even though many of these genes have proposed roles in nuclear mechanics[62, 63, 64], their role in regulating cytoplasmic rheology is not understood. When we tested *GFP:lmn-1/LaminA*, we found generally lower storage and loss moduli over all frequencies (Supp. Data Fig 9a), which was unchanged in day 8 adults. Fitting the fractional Kelvin-Voigt model to the data revealed a strongly reduced cytoplasmic viscosity (embodied in parameter c_β) and a slight but insignificant increase in its elastic response visible in the reduction of the low-frequency exponent α and increase in its prefactor c_α (Supp. Data Fig 9f). We then asked how mutants with defects in coupling chromatin to the envelope affect ageing of the cytoplasm. When we tested *lem-2* and *emr-1* mutant animals as day one adults, we did not observe a major difference in cytoplasmic rheology compared to control cells. Both mutants, however, had a strong effect on cytoplasmic rheology during age, as evidenced by a shift in cross-over frequency (Fig. 5e,f, Supp.

Data Fig. 9) - a value that determines if a material predominantly deforms as a solid or a liquid. In addition, we observed a significantly lower pre-factor c_β in the *emr-1* mutant, indicative for a reduction in viscosity (Fig. 5g). Together with a subtle but insignificant reduction in c_α pre-factor and increase in β exponent, this suggests a general softening and fluidification of the cytoplasm due to the mutations of the nuclear envelope (Supp. Data Fig. 9, Supplementary Text 3). Together, our data show that mutation of the nuclear envelope sensitize the cytoplasm to age-related changes in viscoelasticity.

3 Discussion

Here, we introduced a new active microrheology procedure based on optical gradient traps, optimized for small sample volumes that massively increases experimental throughput by reducing material expenditure, instrumentation complexity and measurement time. The direct, momentum-based force measurements enables these measurements in turbid media with varying refractive index and unknown probe morphology[65], which affords its application inside cells without time consuming calibration routines. Overall, these factors reduce costs and experimental complexities to provide a rich repertoire of parameters for drug screening and model testing.

Our method has significant advantages over existing active rheology routines based on two separate trapping and detection laser[16] or separating one laser beam into two beams with orthogonal polarization[22]. Even though this would fulfil the condition that forces and deformations are measured instantaneously (for equations 1 to be valid without further compensation), this comes with the complexity that requires to align two optical paths and two detectors at the BFP interferometry collecting system. Further, the alignment of two laser beams is not constant over the whole field-of-view of the optical trap, limiting the execution of dynamic trapping experiments at various locations [16, 66]. Moreover, depolarization for light rays propagating at large angles would generate massive crosstalk between the two traps [67, 68], hence the measurements would be affected by depolarization in such a highly focused laser beam [67].

Despite the promised versatility, our approach has some short-comings, that arise from the violation of the time-continuity intrinsic in an AOD-based time-sharing configuration. As extensively laid out

in the Supp Text, the time-sharing measurements cannot unequivocally determine the real-part of the response function in the frequency spectrum of pure and ideal Maxwell liquids in an arbitrarily stiff trap. It is important to emphasize again the fact that for all the samples it is convenient to make the measurements with a trap that is much less rigid than the material behaviour at the Nyquist frequency. That is, one must choose a $k << 1/|\hat{\chi}(\omega_t/2)|$ or equivalently $G_0 << |\hat{G}(\omega_t/2)|$. So in the worst case it will be necessary to make several iterations to find the optimal stiffness of the trap k with which to make the measurements.

Our examples illustrate how a single trap can be used to measure various materials, ranging from simple fluids to the complex response of viscoelastic fluid-like protein condensates and different organelles inside living cells and whole animals. TimSOM correctly measured the previously described Maxwell-like behaviour of biomolecular condensates and their time-dependent rigidity transition with a single trial. Even though this rigidity transition can be identified by the fiber formation in 20% of all droplets[6], microrheology can determine the rigidity transition, even without any visible changes in droplet morphology. We also observed that the shear modulus in the center of the condensates is slightly higher than at the periphery, suggesting a potential mechanism for the rigidity percolation transition. These observations on MEC-2/SH3 co-condensates contrast the observations from other condensates, which are hypothesized to experience an interfacial compaction during maturation[69, 70]. In contrast to the dual trap rheology assay, we should note that bulk rheology is independent of surface tension. Consequently, the low frequency range is not limited by surface effects and can thus be extended, in principle, to ultra-long timescales. We should stress at this point that the surface, or interfacial tension *in vivo* is irrelevant, as the droplet environment inside a cell is different than that of the measurement *in vitro*. Thus, values for surface tension (γ) derived from dual trap experiments *in vitro* should be interpreted with caution. Further, the single trap TimSOM experiments measures the bulk rheology and is thus independent of substrate adhesion of the droplet, which could be the cause of experimental deviations from the expected behaviour in the dual trap assay. Likewise, the experimental routine is much simpler and does not require perfect alignment of the microspheres in the equatorial plane of the droplet. These important simplifications set the base for future implementations of high-throughput rheology measurements and

screening purposes aimed to identified regulators of condensate ageing processes.

A complete understanding of the adaptive response to mechanical requires knowledge of the cell cortex mechanics and ion channel dynamics[71] and the subcellular mechanical properties[72, 73]. We find that the mechanics of the nucleus is dominated by the cytoplasmic/nuclear interface rather than the nucleoplasm. This result coincides with recent observations made with Brillouin microscopy of cells in developing ascidian embryo, where a higher Brillouin shift was observed in perinuclear regions, indicative for a higher longitudinal modulus of the interface, than both, the nucleus and the cytoplasm[74]. Likewise, observations that the nucleus has a lower mass density and longitudinal modulus than the surrounding cytoplasm[75, 58] support our data that nucleoplasm is a soft, viscoelastic solid. Even though our measurements did not reveal significant differences in complex shear moduli between cytoplasm and nucleoplasm, it suggests that the a priori assumption of stiffer nuclei primarily stems from the nuclear interface and the envelope. This observation is consistent with the 'open' state of euchromatin of undifferentiated progenitor cells and future work needs to test how nucleoplasm rheology changes with chromatin compaction in differentiated cells. Our results add to the previous observations that cells primarily respond as fractional Kelvin-Voigt materials[4]. This might have important consequences on the way how cells store and transmit mechanical energy over long time scales and distance, especially for morphodynamic events[7] and mechanosensation[76, 77].

Finally we applied our method to investigate cytoplasmic rheology in a living animal. We found that organismal age subtly increases the fluidity of the cytoplasm, which is increased in mutants of the nuclear envelope. The findings that the nucleus influences cytoplasmic stiffness is similar to glioma cells, in which the stiffness of the cytoplasm correlated with decreased level LaminA/C[10]. The question arises how the envelope coordinates such cytoplasmic changes? It was proposed that the density of ribosomes induce crowding and scale cytoplasmic viscosity[78]. It is conceivable that age reduces the density of ribosomes as the synthesis demand of an animal decreases[79]. Alternatively, mitochondrial morphodynamics and number decrease during age[80, 81], posing a plausible explanation for the age-related decline in viscoelasticity and an exciting novel research direction of the involvement of mitochondria in cell mechanics. Future work needs to address how a change in cytoplasmic viscoelasticity affects

cellular function during age and more general, how genetic factors influence rheological parameters and viscoelasticity.

Acknowledgements We would like to thank the PRBB fish facility for animal maintenance, *Caenorhabditis elegans* center (CGC, supported by the National Institutes of Health, P40 OD010440) for reagents and Neus Sanfeliu-Cerdan for help with sample preparation and comments on the first draft. All authors thank Arnau Farré, the NMSB and Cell Dynamics lab members for discussion. We thank Peter Askjaer for *C. elegans* strains.

Funding MK acknowledges financial support from the ERC (MechanoSystems, 715243),Human Frontiers Science Program (RGP021/2023), MCIN/ AEI/10.13039/501100011033/ FEDER "A way to make Europe" (PID2021-123812OB-I00, CNS2022-135906), "Severo Ochoa" program for Centres of Excellence in R&D (CEX2019-000910-S), from Fundació Privada Cellex, Fundació Mir-Puig, and from Generalitat de Catalunya through the CERCA and Research program. V.R. acknowledges financial support from the Ministerio de Ciencia y Innovacion through the Plan Nacional (PID2020-117011GB-I00) and funding from the European Union's Horizon EIC-ESMEA Pathfinder program under grant agreement No 101046620. XS acknowledges funding from AGAUR (2017 SGR 324), MINECO (BIO2015-70092-R and PID2019-110198RB-I00), and the European Research Council (CONCERT, contract number 648201). CGC acknowledges a graduate fellowship from MINECO (PRE2018-084684). IRB Barcelona and ICFO are the recipient of a Severo Ochoa Award of Excellence from MINECO (Government of Spain).

Author contributions statement FCC performed *in silico* and experimental characterization of TimSOM, optical trapping simulations and biomolecular condensate microrheology. SOV did experimental characterization of TimSOM, zebrafish microinjection, intracellular and intranuclear microrheology. CMF performed strain generation through CRISPR-Cas9, *in vitro* and *in vivo* analysis of *C. elegans* lipid droplets and intestinal microrheology. FP and SJ generated zebrafish strains and performed the cloning for mRNA used for microinjection. CGC established MEC-2::UNC-89 co-condensates for *in vitro* char-

acterizations of biomolecular condensates. XS, VR and MK were responsible for funding acquisition. PAF developed the theoretical compensation pipeline, performed simulations and experiments on model materials. FCC, PAF and MK conceived the idea and wrote the manuscript, with input from all authors.

Competing Interest PAF is holder of the patent #WO/2022/171898 protecting the time-shared rheology technique[82]. XS is cofounder of Nuage Therapeutics. All other authors do not declare any conflicts of interests.

Figures

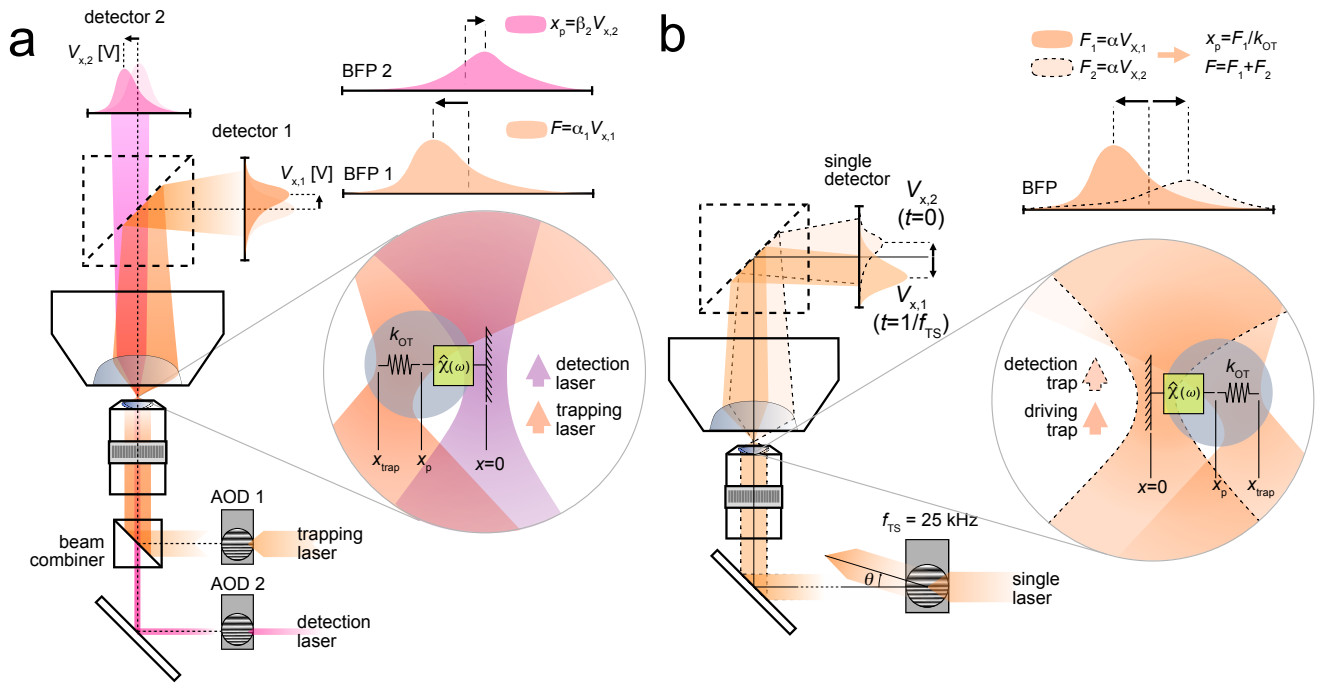

Fig. 1. Time-sharing optical microrheology. a, Schematic of an optical microrheology set-up consisting of two coaxial lasers and two detectors. The *trapping* laser (orange) exerts optical forces onto the rheological probe, giving rise to light momentum changes that are directly measured by detector 1 as $F_x = \alpha_1 V_{x,1}$ (same for Y). In turn, the BFP interferometry pattern of the *detection* laser (pink) is tracked by detector 2 to measure probe displacements as $x_p = \beta_2 V_{x,2}$ (same for Y). The two beams are combined before the microscope objective and split after the collecting lens with the respective dichroic cubes. **b,** Schematic of time-shared optical microrheology with direct light momentum sensing of optical forces. A single 1064-nm laser beam is time-shared at 25 kHz between a *driving* (1) and a *detection* (2) trap. The driving trap (orange) oscillates around the trapped particle, while the detection trap (light orange, dashed line) monitors the particle position as $x_p = F_1/k_{OT}$. The optical force acting onto the probe particle corresponds to the addition of forces exerted by the two traps: $F = F_1 + F_2$, which are obtained as $F_{1,2} = \alpha V_{1,2}$, where $alpha$ is here the volt-to-picoNewton conversion factor of a single, light-momentum direct force sensor.

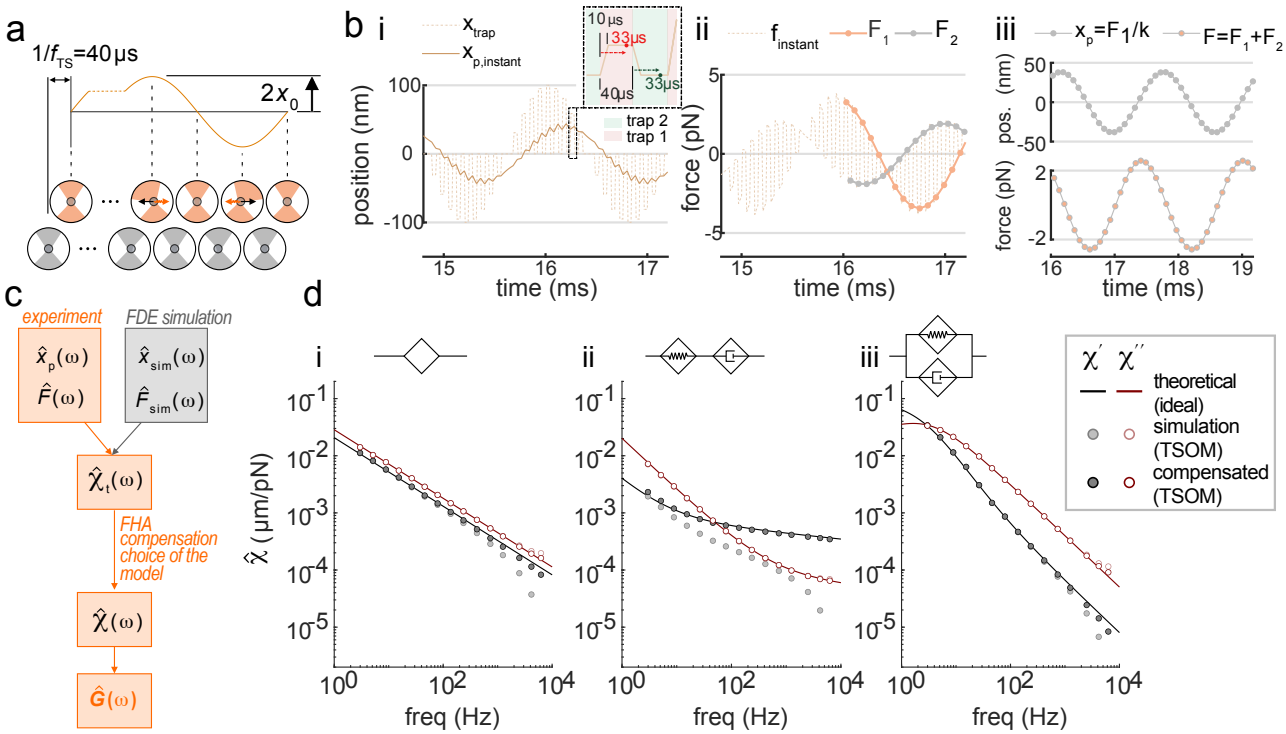

Fig. 2. Quantitative description of bead motion in TimSOM. a, Time-sharing position and force measurement sequence. While trap 2 remains motionless at the optical axis in order to detect bead displacements through BFP interferometry, trap 1 applies an active sinusoidal perturbation with amplitude $2x_0$ at the time sharing frequency $1/f_{TS}$. The schematic on the bottom represents the deflection of the laser beam by the trapped particle for the active (orange) and passive trap (grey). **b,** Simulation of the instantaneous position (i) of the probe particle in water using the *fractional derivative equation* method ($A = 100$ nm, $f = 625$ Hz, $k = 50$ pN/µm, water viscosity: $\eta = 10^{-3}$ Pa·s) and the resulting instantaneous optical force acting onto the probe (ii). Interleaved force values for the detection and driving traps, sampled at $f_{TS}/2 = 12.5$ Hz with a delay of 33 µs (Supplementary Text), are indicated as thin dashed line. Inset of (i) shows the time sharing properties of the active (trap 1) and passive trap (trap 2) with the rise time of 10µs. In iii, the probe position and the total force are shown. **c,** Analytical pipeline to retrieve the G modulus from the deviated measurements and/or simulations. **d,** i, storage and loss G moduli for a single springpot with $c = 1$ and $\alpha = 0.6$. Solid lines correspond to the theoretical model, $G^*(\omega) = c(i\omega)^\alpha$, while light dots represent the measurement deviation due to TimSOM simulated using the FDE method and dark dots represent the corrected compensation values retrieved through the FHA pipeline. In ii and iii, same for the fractional Maxwell model ($c_1 = 100$, $\alpha_1 = 0.1$, $c_2 = 1$, α_2=0.9) and the fractional Kelvin-Voigt model ($c_1 = 1$, $\alpha_1 = 0.1$, $c_2 = 0.1$, α_2=0.9).

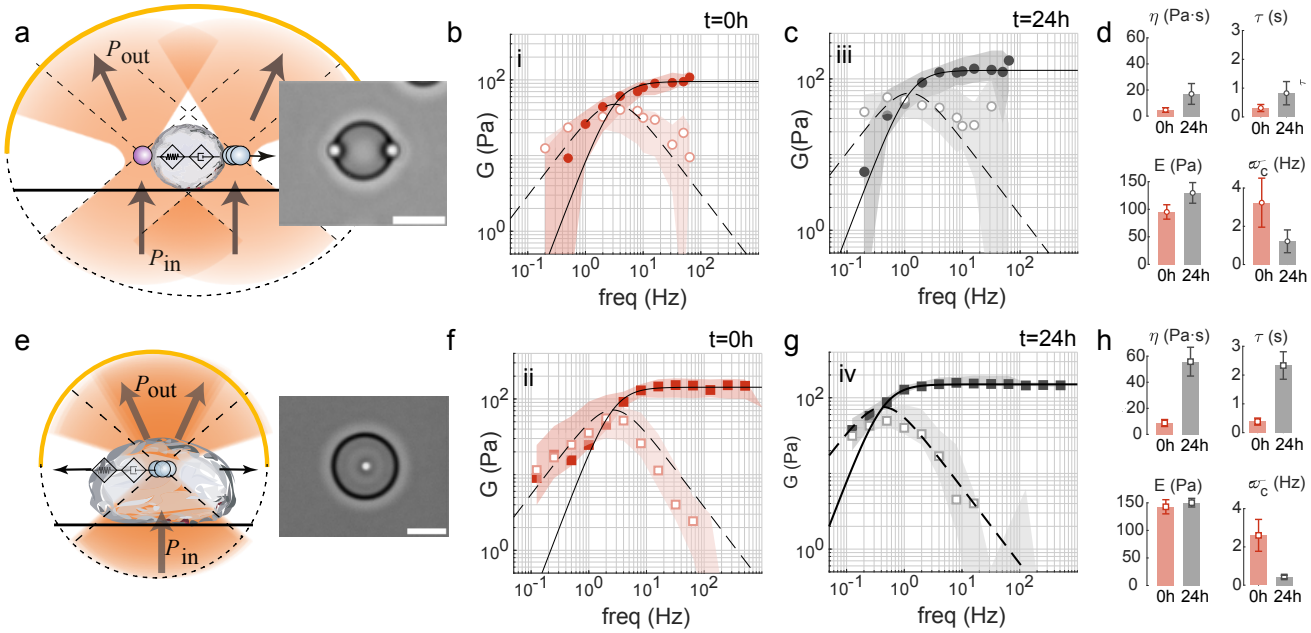

Fig. 3. Viscoelastic properties of biomolecular condensates. a, Schematic and snapshot of a MEC-2/UNC-89 protein droplet squeezed by a pair of optically trapped PEG-terminated microbeads in a dumbbell configuration. Scale bar = 10 µm. P_{in}, P_{out} define the light momentum before and after interacting with the trapped microsphere. **b, c,** Storage ($G'(\omega)$, filled circles) and loss ($G''(\omega)$, open circles) moduli measured in the dumbbell configurations at (b) $t = 0h$ and (c) $t = 24h$ after condensate formation. The solid and dashed lines are the real and imaginary parts of a non-fractional Maxwell G modulus fitted to the acquired data. Circles and shadows are the median and $\pm 25\%$ quantiles over N=10 (b) and N=9 (c) measurements. **d,** Variation of the fitting parameters showing the change in the dynamic viscosity, η (Pa·s), stiffness, E (Pa), time constant, $\tau = \eta/E$ (s) and crossover frequency, $\omega_c = 1/\tau$ (Hz) over 24h condensate maturation in the dumbbell configuration. The significant decrease in ω_c demonstrates the maturation accelerated by the MEC-2/UNC-89 co-condensation as described[6]. **e,** Schematic and snapshot of a MEC-2/UNC-89 protein droplet with an embedded carboxylated microbead, used as probe for time-shared optical tweezer microrheology. **f, g,** Storage ($G'(\omega)$, filled squares) and loss ($G''(\omega)$, open squares) moduli measured with TimSOM at (b) $t = 0h$ and (c) $t = 24h$ after condensate formation. The solid and dashed lines are the real and imaginary parts of a non-fractional Maxwell G modulus fitted to the acquired data. Squares and shadows are the median and $\pm 25\%$ quantiles over N=5 (b) and N=5 (c) measurements. **d,** Variation of the fitting parameters over 24h extracted from the TimSOM routine. The significant decrease in ω_c demonstrates the maturation accelerated by the MEC-2/UNC-89 co-condensation as described[6].

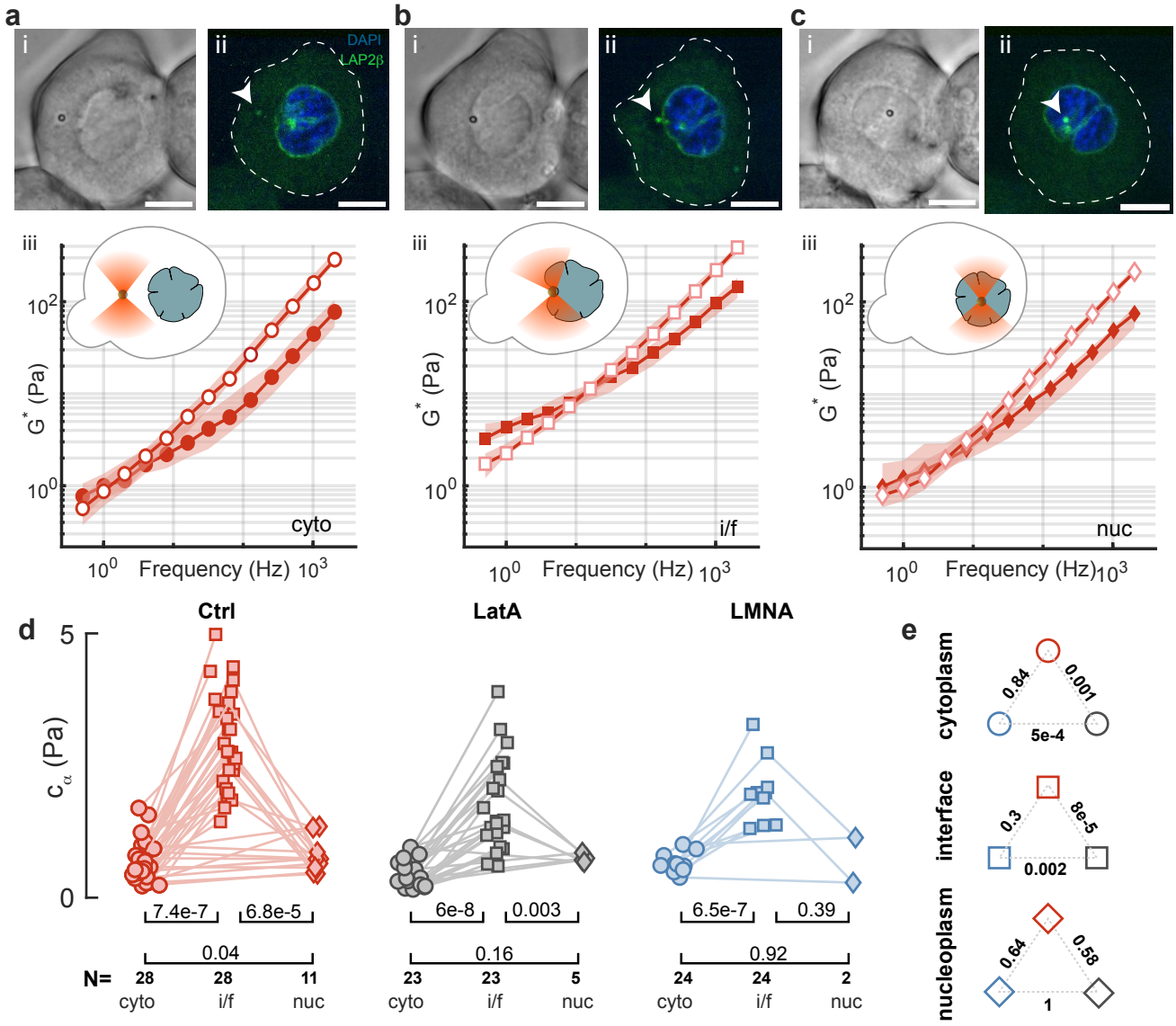

Fig. 4. Cytoplasm versus nuclear rheology. a-c, Representative (i) brightfield and (ii) confocal imaging of a zebrafish progenitor cell expressing Lap2β:GFP with a microsphere in its (a) cytoplasm (cyto), (b) nuclear interface (i/f) and (c) inside the nucleus (nuc). (iii) Frequency spectrum of the complex G modulus indicating the storage (closed symbols) and loss modulus (open symbols) of the three corresponding compartments. Solid line is a fit of the fractional Kelvin-Voigt model to the data. Scale bars = 10µm. **d,** Stiffness (C_α) of the cytoplasm, nuclear interface and nucleoplasm for control and actin depolymerization (LatA) conditions as extracted from the fit of a fractional Kelvin-Voigt model to the rheological spectrum. Lines connect paired datapoints that were acquired in the same cell with the same microsphere. p-values above the brackets derived from a paired t-test. See Supp. Data Fig. 4 and Supplementary Table 1 for the comparison of all other fit parameters and their p-values. N=number of cells used in the measurement. **e,** p-values of the indicated pairwise comparison of C_α of the cytoplasm, nuclear interface and the nucleoplasm in control, LatA treatment and laminA (LMNA) overexpression.

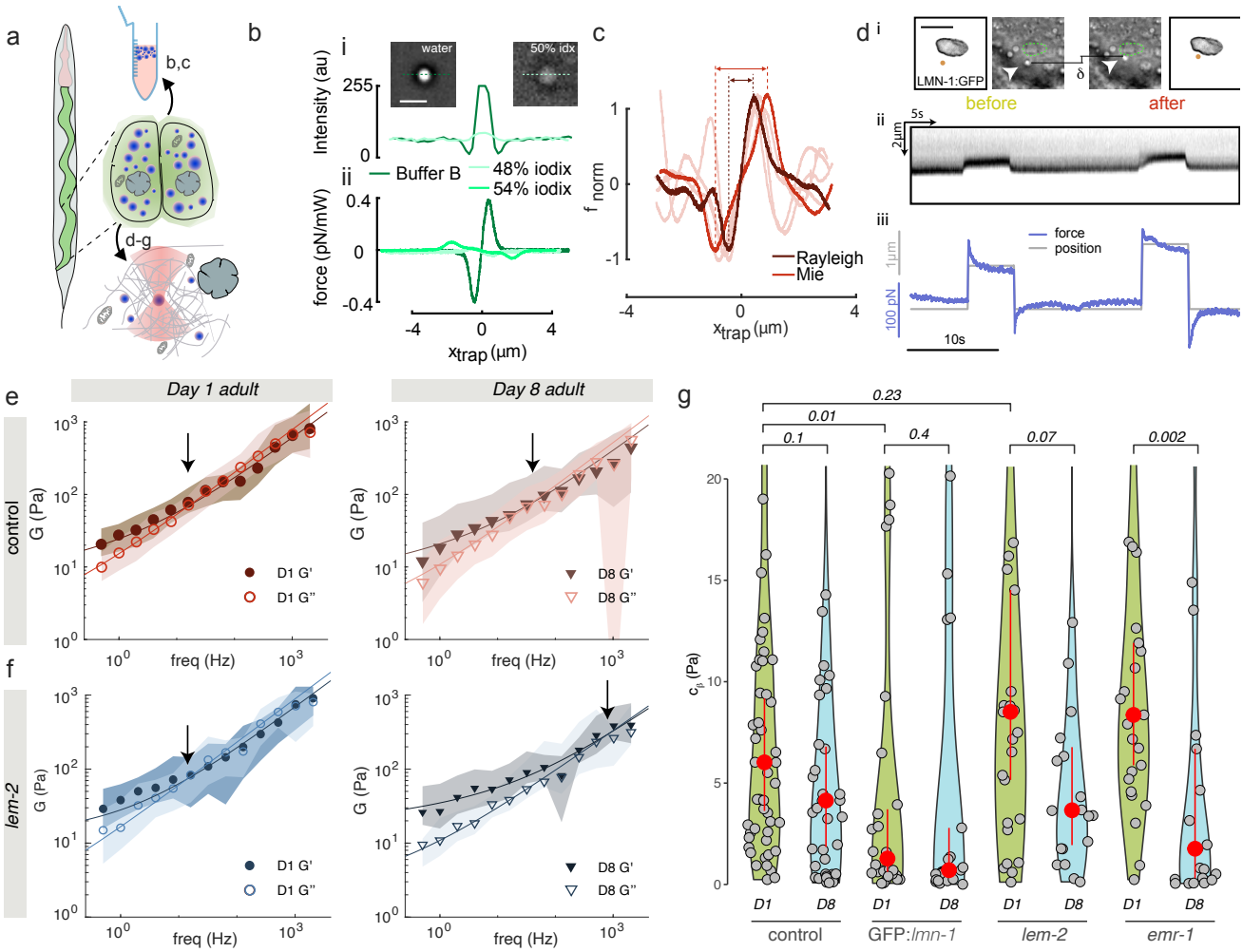
a
b,c
d-g
b
i
water
50% idx
Intensity (au)
255
0
ii
Buffer B
48% iodix
54% iodix
force (pN/mW)
0.4
0
-0.4
-4
0
4
xtrap (μm)
c
f norm
1
0
-1
Rayleigh
Mie
xtrap (μm)
d i
LMN-1:GFP
before
after
δ
ii
5s
2μm
iii
force
position
1μm
100 pN
10s
e
Day 1 adult
Day 8 adult
control
G (Pa)
D1 G'
D1 G''
D8 G'
D8 G''
freq (Hz)
f
lem-2
g
0.23
0.01
0.1
0.4
0.07
0.002
c_β (Pa)
D1
D8
control
GFP:lmn-1
lem-2
emr-1

Fig. 5 ***(preceding page).*** **Longitudinal tissue microrheology** ***in vivo*****. a,** Sketch of an animal with the intestinal tissue highlighted in green and the pharynx in red. The close-up sketch shows a pair of posterior intestinal cells with lipid droplets in blue. Lipid droplets were isolated from adult animals, purified and tested under various conditions for their suitability as optical tweezer probes (b,c see Methods). For *in vivo*, individual droplets were trapped to measure the rheological response of the material in its vicinity (panels d-g). **b,** Refractive index matching with varying concentrations of iodixanol. (i) Brightfield micrograph of a lipid droplet in buffer B on the left (see Methods, representative for N=6 droplets) and in 48% of iodixanol (right, N=12). Graph shows the intensity profile along the dotted line indicated in the photograph. Scale bar = 2µm. (ii) Force profile on a droplet in the matched conditions, for 0, 48% and 54% of iodixanol. **c,** Force scan across the lipid droplet for particle radius estimation (see Methods). Lipid droplets vary in size from the trapping force Rayleigh (dark red) and Mie (light red) limits. N=2 droplets, representative for all measurements. **d,** (i) Fluorescence of *GFP::lmn-1* and bright field images demonstrating nuclear deformation with a trapped lipid droplet upon contact during a tweezer experiment. δ indicates the deformation of the nucleus during the test, arrowhead points to the trapped lipid droplet. Scale bar = 2µm. (ii) Kymograph of two consecutive step indentations of an intestinal nucleus using a lipid droplet as force probe. (iii) Force and displacement during the same step indentation protocol. **e, f,** Frequency dependent shear modulus for two different ages of (e) wildtype and (f) age-matched *lem-2* mutants. The median and $\pm 25\%$quantiles are represented by lines and shadows, respectively. **g,** Viscosity (C_β) of the cytoplasm as extracted from the high-frequency component derived from the fit of the fractional Kelvin-Voigt model to the rheological spectrum of day-1 and day-8 adults for four different genotypes as indicated. Red circle indicates median$\pm$bootstrapped 95% confidence interval. p=0.003 derived from a non-parametric Kruskal-Wallis test, followed by a pairwise comparison using a one-sided Dunn test as indicated above the horizontal brackets (for details on statistics and number of measurements see Supplementary Data Table 2 and Supp. Data Fig. 9).

References

[1] HARRISON, V. G. W., The Science of Rheology. *Nature* **146**, 580–582 (1940).

[2] Petridou, N. I., Heisenberg, C., Tissue rheology in embryonic organization. *The EMBO Journal* **38**, 1–13 (2019).

[3] Han, Y. L., et al., Cell swelling, softening and invasion in a three-dimensional breast cancer model. *Nature Physics* **16**, 101–108 (2020).

[4] Hurst, S., Vos, B. E., Brandt, M., Betz, T., Intracellular softening and increased viscoelastic fluidity during division. *Nature Physics* **17**, 1270–1276 (2021).

[5] Lange, J. R., Fabry, B., Cell and tissue mechanics in cell migration. *Experimental Cell Research* **319**, 2418–2423 (2013).

[6] Sanfeliu-cerdán, N., et al., A MEC-2 / stomatin condensate liquid-to-solid phase transition controls neuronal mechanotransduction during touch sensing. *Nature Cell Biology* **89** (2023).

[7] Venturini, V., et al., The nucleus measures shape changes for cellular proprioception to control dynamic cell behavior. *Science* **370**, eaba2644 (2020).

[8] Mathieu, S., Manneville, J. B., Intracellular mechanics: connecting rheology and mechanotransduction. *Current Opinion in Cell Biology* **56**, 34–44 (2019).

[9] Svoboda, K., Schmidt, C., Schnapp, B., Block, S., Direct observation of kinesin stepping by optical trapping interferometry © 1993 Nature Publishing Group. *Nature* **365**, 721–728 (1993).

[10] Alibert, C., et al., Multiscale rheology of glioma cells. *Biomaterials* **275**, 120903 (2021).

[11] Hall, C. M., Moeendarbary, E., Sheridan, G. K., Mechanobiology of the brain in ageing and Alzheimer's disease. *European Journal of Neuroscience* **53**, 3851–3878 (2021).

[12] Krieg, M., et al., Genetic defects in β-spectrin and tau sensitize C. elegans axons to movement-induced damage via torque-tension coupling. *eLife* **6**, e20172 (2017).

[13] Patel, A., et al., A Liquid-to-Solid Phase Transition of the ALS Protein FUS Accelerated by Disease Mutation. *Cell* **162**, 1066–1077 (2015).

[14] Jawerth, L., et al., Protein condensates as aging Maxwell fluids. *Science* **370**, 1317–1323 (2020).

[15] Ebata, H., et al., Activity-dependent glassy cell mechanics I : Mechanical properties measured with active microrheology. *bioRxiv* **null**, null (2023).

[16] Blehm, B. H., Devine, A., Staunton, J. R., Tanner, K., In vivo tissue has non-linear rheological behavior distinct from 3D biomimetic hydrogels, as determined by AMOTIV microscopy. *Biomaterials* **83**, 66–78 (2016).

[17] Staunton, J. R., Blehm, B., Devine, A., Tanner, K., In situ calibration of position detection in an optical trap for active microrheology in viscous materials. *Optics Express* **25**, 1746 (2017).

[18] Alshareedah, I., et al., Sequence-encoded grammars determine material properties and physical aging of protein condensates. *BioRxiv* 1–23 (2023).

[19] Català-Castro, F., Schäffer, E., Krieg, M., Exploring cell and tissue mechanics with optical tweezers. *Journal of cell science* **135** (2022).

[20] Visscher, K., Gross, S. P., Block, S. M., Construction of multiple-beam optical traps with nanometer-resolution position sensing. *IEEE Journal on Selected Topics in Quantum Electronics* **2**, 1066–1076 (1996).

[21] Brau, R. R., et al., Passive and active microrheology with optical tweezers. *Journal of Optics A: Pure and Applied Optics* **9** (2007).

[22] Moffitt, J. R., Chemla, Y. R., Izhaky, D., Bustamante, C., Differential detection of dual traps improves the spatial resolution of optical tweezers. *Proceedings of the National Academy of Sciences of the United States of America* **103**, 9006–9011 (2006).

[23] Farré, A., Montes-Usategui, M., A force detection technique for single-beam optical traps based on direct measurement of light momentum changes. *Optics Express* **18**, 11955 (2010).

[24] Farré, A., Marsà, F., Montes-Usategui, M., Optimized back-focal-plane interferometry directly measures forces of optically trapped particles. *Optics Express* **20**, 12270 (2012).

[25] Thalhammer, G., Obmascher, L., Ritsch-Marte, M., Direct measurement of axial optical forces. *Optics Express* **23**, 6112 (2015).

[26] Bui, A. A., et al., Calibration of force detection for arbitrarily shaped particles in optical tweezers. *Scientific Reports* **8**, 1–12 (2018).

[27] Gittes, F., Schmidt, C. F., Interference model for back-focal-plane displacement detection in optical tweezers. *Optics Letters* **23**, 7 (1998).

[28] Vermeulen, K. C., et al., Calibrating bead displacements in optical tweezers using acousto-optic deflectors. *Review of Scientific Instruments* **77**, 1–6 (2006).

[29] Català-Castro, F., Venturini, V., Ortiz-Vásquez, S., Ruprecht, V., Krieg, M., Direct force measurements of subcellular mechanics in confinement using optical tweezers. *Journal of Visualized Experiments* **2021**, 1–35 (2021).

[30] Yu, L., Sheng, Y., Mechanical analysis of the optical tweezers in time-sharing regime. *Optics Express* **22**, 7953 (2014).

[31] Martínez, I. A., Petrov, D., Force mapping of an optical trap using an acousto-optical deflector in a time-sharing regime. *Applied Optics* **51**, 5522–5526 (2012).

[32] Ren, Y., Wu, J., Zhong, M., Li, Y., Monte-Carlo simulation of ef fective stif fness of time-sharing optical tweezers. *CHINESE OPTICS LETTERS* **8**, 170–172 (2010).

[33] Deng, L., et al., Fast and slow dynamics of the cytoskeleton. *Nature Materials* **5**, 636–640 (2006).

[34] Bonfanti, A., Kaplan, J. L., Charras, G., Kabla, A., Fractional viscoelastic models for power-law materials. *Soft Matter* **16**, 6002–6020 (2020).

[35] Evans, R. M., Tassieri, M., Auhl, D., Waigh, T. A., Direct conversion of rheological compliance measurements into storage and loss moduli. *Physical Review E - Statistical, Nonlinear, and Soft Matter Physics* **80**, 8–11 (2009).

[36] Placet, V., Delobelle, P., Mechanical properties of bulk polydimethylsiloxane for microfluidics over a large range of frequencies and aging times. *Journal of Micromechanics and Microengineering* **25**, 1–8 (2015).

[37] Brangwynne, C. P., et al., Germline P Granules Are Liquid Droplets That Localize by Controlled Dissolution/Condensation. *Science* **5** (2009).

[38] Banani, S. F., Lee, H. O., Hyman, A. A., Rosen, M. K., Biomolecular condensates: Organizers of cellular biochemistry. *Nature Reviews Molecular Cell Biology* **18**, 285–298 (2017).

[39] Mathieu, C., Pappu, R. V., Paul Taylor, J., Beyond aggregation: Pathological phase transitions in neurodegenerative disease. *Science* **370**, 56–60 (2020).

[40] Sanfeliu-Cerdán, N., Lin, L.-C., Dunn, A. R., Goodman, M. B., Krieg, M., Visualizing Neurons Under Tension In Vivo with Optogenetic Molecular Force Sensors. *Methods in molecular biology (Clifton, N.J.)* **2600**, 239–266 (2023).

[41] Jawerth, L. M., et al., Salt-Dependent Rheology and Surface Tension of Protein Condensates Using Optical Traps. *Physical Review Letters* **121**, 258101 (2018).

[42] Jun, Y., Tripathy, S. K., Narayanareddy, B. R., Mattson-Hoss, M. K., Gross, S. P., Calibration of optical tweezers for in vivo force measurements: How do different approaches compare? *Biophysical Journal* **107**, 1474–1484 (2014).

[43] Srivastava, L. K., Ju, Z., Ghagre, A., Ehrlicher, A. J., Spatial distribution of lamin A/C determines nuclear stiffness and stress-mediated deformation. *Journal of Cell Science* **134**, 1–7 (2021).

[44] Guilak, F., Tedrow, J. R., Burgkart, R., Viscoelastic properties of the cell nucleus. *Biochemical and Biophysical Research Communications* **269**, 781–786 (2000).

[45] White, R. J., et al., A high-resolution mRNA expression time course of embryonic development in zebrafish. *eLife* **6**, 1–32 (2017).

[46] Farrell, J. A., et al., Single-cell reconstruction of developmental trajectories during zebrafish embryogenesis. *Science* **360** (2018).

[47] Davidson, P. M., Cadot, B., Actin on and around the Nucleus. *Trends in Cell Biology* **31**, 211–223 (2021).

[48] Diz-Muñoz, A., et al., Control of directed cell migration in vivo by membrane-to-cortex attachment. *PLoS Biology* **8**, e1000544 (2010).

[49] Kenyon, C., Jean, C., Grensch, E., Adam, R., Ramon, T., A C.elegans mutant that twice as long as wild type. *Nature* **366**, 461–464 (1993).

[50] Ivanovska, I. L., Tobin, M. P., Bai, T., Dooling, L. J., Discher, D. E., Small lipid droplets are rigid enough to indent a nucleus, dilute the lamina, and cause rupture. *The Journal of cell biology* **222** (2023).

[51] E., L. A., et al., Lipid droplets are intracellular mechanical stressors that impair hepatocyte function. *Proceedings of the National Academy of Sciences* **120**, e2216811120 (2023).

[52] Mosquera, J. V., Bacher, M. C., Priess, J. R., Nuclear lipid droplets and nuclear damage in Caenorhabditis elegans. *PLoS Genetics* **17** (2021).

[53] Bormuth, V., et al., Optical trapping of coated microspheres. *Opt Express* **16**, 13831–13844 (2008).

[54] Ding, Y., et al., Isolating lipid droplets from multiple species. *Nature Protocols* **8**, 43–51 (2013).

[55] Boothe, T., et al., A tunable refractive index matching medium for live imaging cells, tissues and model organisms. *eLife* **6**, 1–15 (2017).

[56] Chowdhury, S., et al., High-resolution 3D refractive index microscopy of multiple-scattering samples from intensity images. *Optica* **6**, 1211 (2019).

[57] Nieminen, T. A., et al., Optical tweezers computational toolbox. *Journal of Optics A: Pure and Applied Optics* **9** (2007).

[58] Remer, I., Shaashoua, R., Shemesh, N., Ben-Zvi, A., Bilenca, A., High-sensitivity and high-specificity biomechanical imaging by stimulated Brillouin scattering microscopy. *Nature Methods* **17**, 913–916 (2020).

[59] Yang, F., et al., Pulsed stimulated Brillouin microscopy enables high-sensitivity mechanical imaging of live and fragile biological specimens. *bioRxiv* 2022.11.10.515835 (2022).

[60] Cohen-Fix, O., Askjaer, P., Cell biology of the Caenorhabditis elegans nucleus. *Genetics* **205**, 25–59 (2017).

[61] Roux, K. J., Burke, B., Nuclear envelope defects in muscular dystrophy. *Biochimica et Biophysica Acta - Molecular Basis of Disease* **1772**, 118–127 (2007).

[62] Fernandez, A., Bautista, M., Wu, L., Pinaud, F., Emerin self-assembly and nucleoskeletal coupling regulate nuclear envelope mechanics against stress. *Journal of cell science* **135** (2022).

[63] Stephens, A. D., Banigan, E. J., Adam, S. A., Goldman, R. D., Marko, J. F., Chromatin and lamin a determine two different mechanical response regimes of the cell nucleus. *Molecular Biology of the Cell* **28**, 1984–1996 (2017).

[64] Ross, J. A., et al., Lem2 is essential for cardiac development by maintaining nuclear integrity. *Cardiovascular Research* **44**, 1–15 (2023).

[65] Català, F., Marsà, F., Montes-Usategui, M., Farré, A., Martín-Badosa, E., Extending calibration-free force measurements to optically-trapped rod-shaped samples. *Scientific Reports* **7**, 1–10 (2017).

[66] Volpe, G., et al., Roadmap for Optical Tweezers. *arXiv* (2021).

[67] Marsà, F., Farré, A., Martín-Badosa, E., Montes-Usategui, M., Holographic optical tweezers combined with back-focal-plane displacement detection. *Optics Express* **21**, 30282 (2013).

[68] Mangeol, P., Bockelmann, U., Interference and crosstalk in double optical tweezers using a single laser source. *Review of Scientific Instruments* **79** (2008).

[69] Shen, Y., et al., Solid/liquid coexistence during aging of FUS condensates. *Bioarxiv* (2022).

[70] Garaizar, A., et al., Aging can transform single-component protein condensates into multiphase architectures. *Proceedings of the National Academy of Sciences of the United States of America* **119**, 1–11 (2022).

[71] Matthews, B. D., Cellular adaptation to mechanical stress: role of integrins, Rho, cytoskeletal tension and mechanosensitive ion channels. *Journal of Cell Science* **119**, 508–518 (2006).

[72] Heo, S. J., Cosgrove, B. D., Daiv, E. N., Mauck, R. L., Mechano-adaptation of the stem cell nucleus. *Nucleus* **9**, 9–19 (2018).

[73] Kirby, T. J., Lammerding, J., Emerging views of the nucleus as a cellular mechanosensor. *Nature Cell Biology* **20**, 373–381 (2018).

[74] Bevilacqua, C., et al., High-resolution line-scan Brillouin microscopy for live imaging of mechanical properties during embryo development. *Nature Methods* **20**, 755–760 (2023).

[75] Schürmann, M., Scholze, J., Müller, P., Guck, J., Chan, C. J., Cell nuclei have lower refractive index and mass density than cytoplasm. *Journal of biophotonics* **9**, 1068–1076 (2016).

[76] Krieg, M., Dunn, A. R., Goodman, M. B., Mechanical control of the sense of touch by β-spectrin. *Nature Cell Biology* **16**, 224–233 (2014).

[77] Das, R., et al., An asymmetric mechanical code ciphers curvature-dependent proprioceptor activity. *Science Advances* **7**, 1–20 (2021).

[78] Delarue, M., et al., mTORC1 Controls Phase Separation and the Biophysical Properties of the Cytoplasm by Tuning Crowding. *Cell* **174**, 338–349.e20 (2018).

[79] Kim, H. S., Pickering, A. M., Protein translation paradox: Implications in translational regulation of aging. *Frontiers in Cell and Developmental Biology* **11**, 1–10 (2023).

[80] Herbener, G. H., A Morphometric Study of Age-Dependent Changes in Mitochondrial Populations of Mouse Liver and Heart1. *Journal of Gerontology* **31**, 8–12 (1976).

[81] Liu, Y. J., McIntyre, R. L., Janssens, G. E., Houtkooper, R. H., Mitochondrial fission and fusion: A dynamic role in aging and potential target for age-related disease. *Mechanisms of Ageing and Development* **186**, 111212 (2020).

[82] Frigeri, P., METHOD AND DEVICE FOR PERFORMING MICRORHEOLOGICAL MEASUREMENTS IN A VISCOELASTIC MEDIUM (2022).

4 Supplementary Data Figures

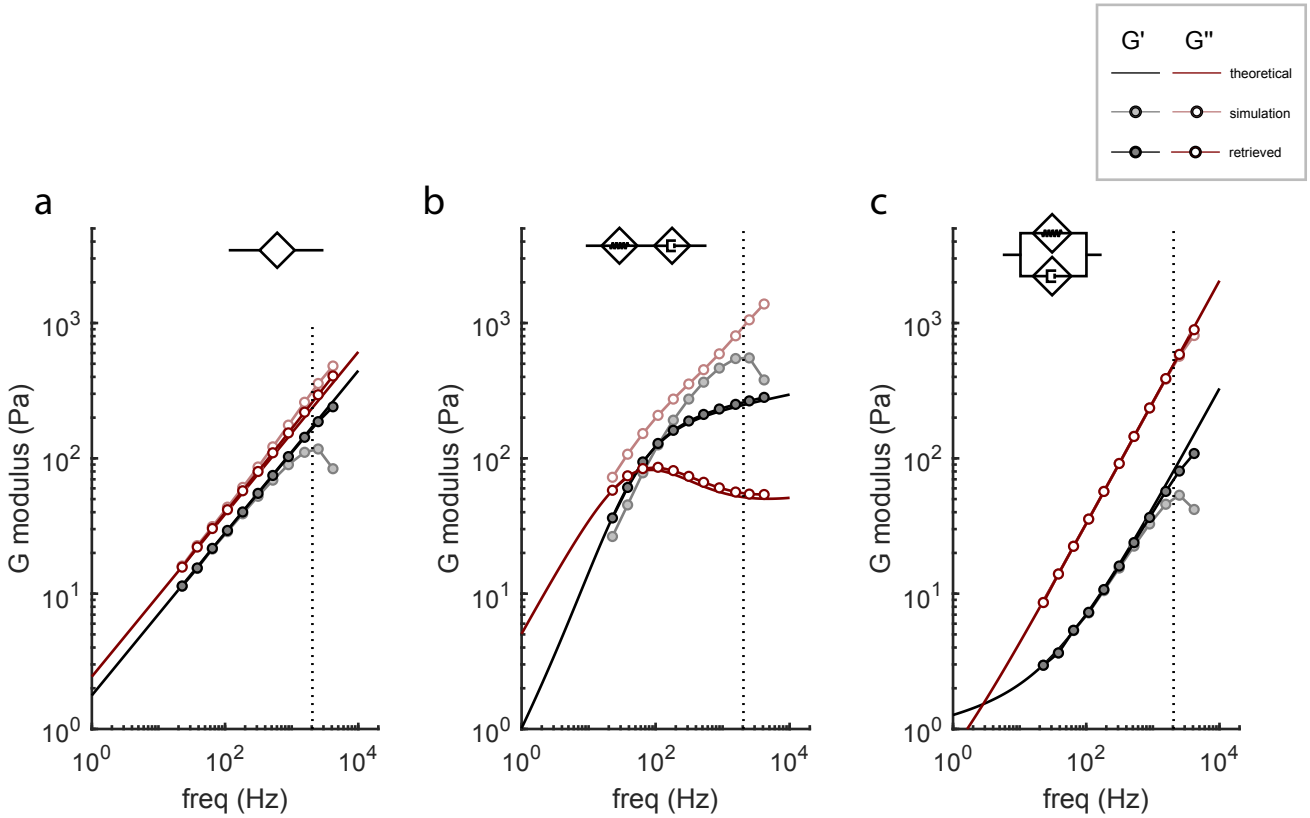

Supp. Data Fig. 1. Compensation of the G modulus extracted from TimSOM. G moduli calculated from the response function, $G^*(\omega) = \frac{1}{6\pi R \chi^*(\omega)}$, simulated through the FDE method for the single spring-pot model, the fractional Maxwell and the fractional Kelvin-Voigt model.

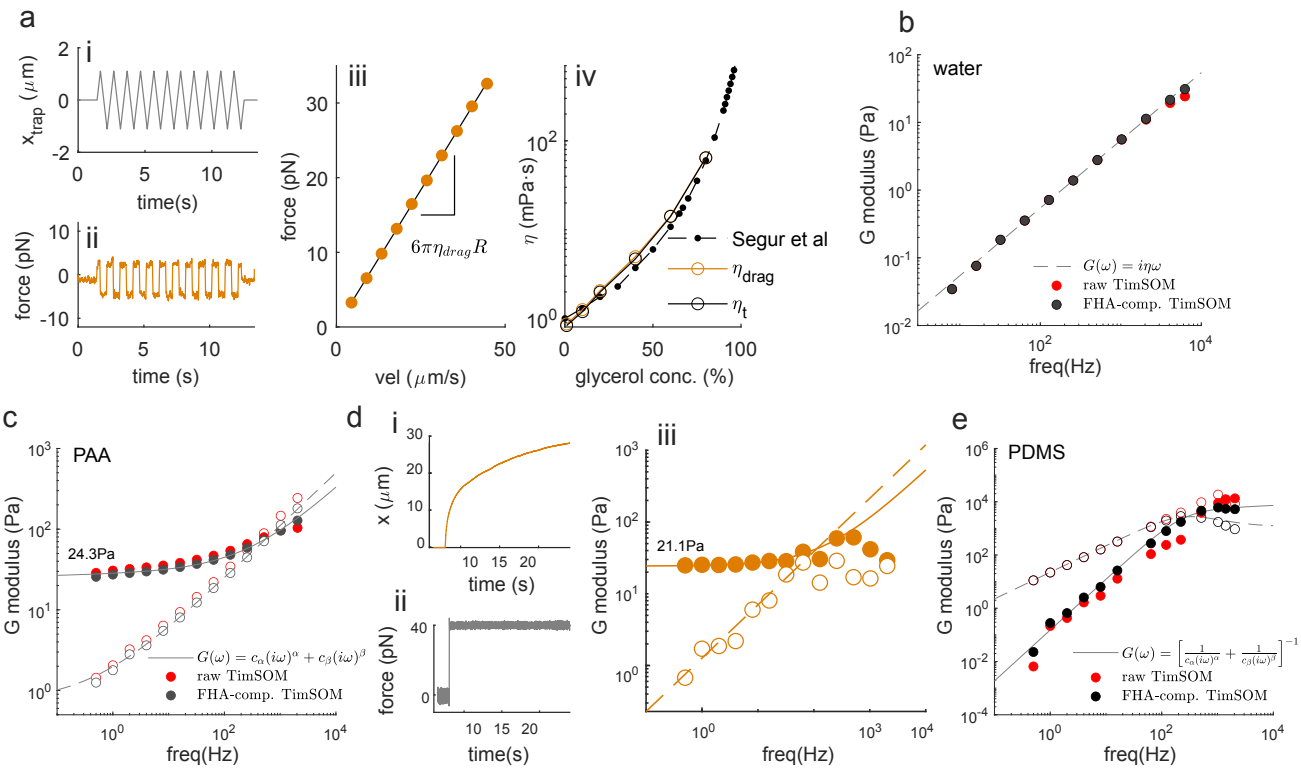

Supp. Data Fig. 2. TimSOM accurately measures viscous and viscoelastic properties. a, Example of a triangular trajectory (i) used to generate constant drag forces (ii) to measure the viscosity of a purely viscous material. Viscosity was obtained from a linear fit (solid line, iii) to the averaged force values obtained for a series of triangles with different velocities (orange dots, iii). The drag force method, η_{drag}, matched the values obtained with TimSOM, η', with glycerol concentrations up to 80% (iv). **b,c** Exemplary raw data of the G modulus obtained through Equation 1 and compensation using the FHA method (Equation 46, in Supplementary Text) for water (b), soft PAA gel (c) and PDMS (e). In all sub-panels, the raw measurement is plotted in red dots and the compensated data is plotted using black dots. Filled (open) circles correspond to the real (imaginary) part. The solid (dashed) lines are the real (imaginary) part of the models specified in the legends. For PAA gel, using the TimSOM method: Using the $J(t) \rightarrow \hat{G}(\omega)$ method: $c_\alpha = 24.3 \pm 1.28$ Pa (CI 95%). **d,** Force clamp experiment to retrieve the G modulus of the same PAA gel as in panel c. The creep motion of the trapped bead ($J(t)$, i) upon a feedback-controlled constant force ($F_0 = 40$ pN, ii) can be used to retrieve the frequency-dependent G modulus. Real (imaginary) part of the G modulus is plotted with filled (open) circles for the experimental retrieval of $G(\omega)$ and with solid (dashed) line for a fit using the Fractional Kelvin-Voigt model. Using the $J(t) \rightarrow \hat{G}(\omega)$ method: $c_\alpha = 21.1 \pm 8.83$ Pa (CI 95%). **e** Exemplary raw data of the G modulus obtained through Equation 1 and compensation using the FHA method (Equation 46, in Supplementary Text) for PDMS. Raw measurement is plotted in red dots and the compensated data is plotted using black dots. Filled (open) circles correspond to the real (imaginary) part. The solid (dashed) lines are the real (imaginary) part of the models specified in the legends.

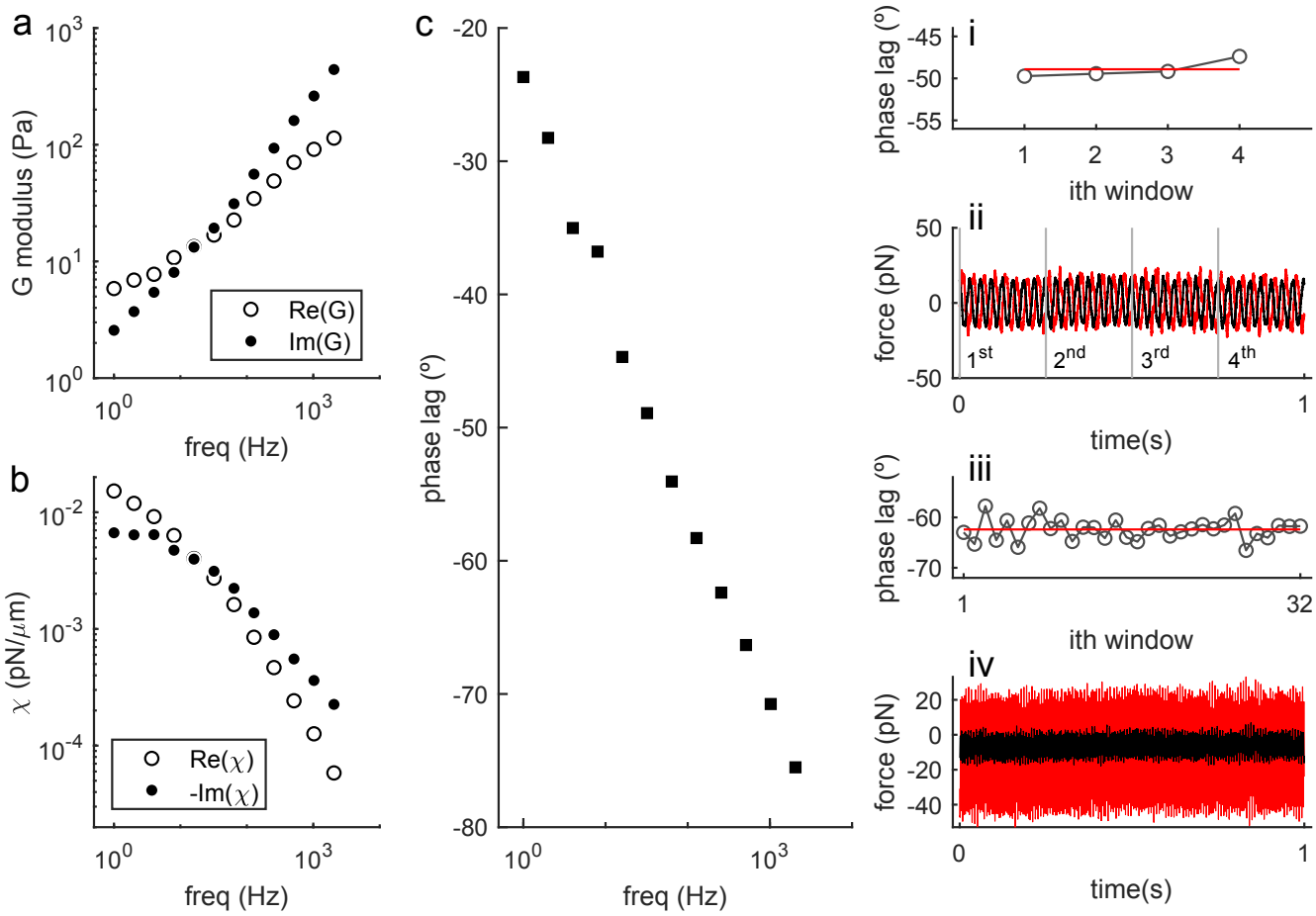

Supp. Data Fig. 3. Performing the rheology routine does not induce phase lag difference. a, b, Representative measurement of the response function (a) and G modulus (b) on a microsphere in the cytoplasm of a zebrafish embryonic cell. **c,** Phase lag between the position and the force oscillatory signals. In inset i, the phase lag over consecutive time windows containing 8 cycles (inset ii) is shown for the oscillation at 32 Hz. In insets iii and iv, same as in i and ii, for the oscillation at 256 Hz.

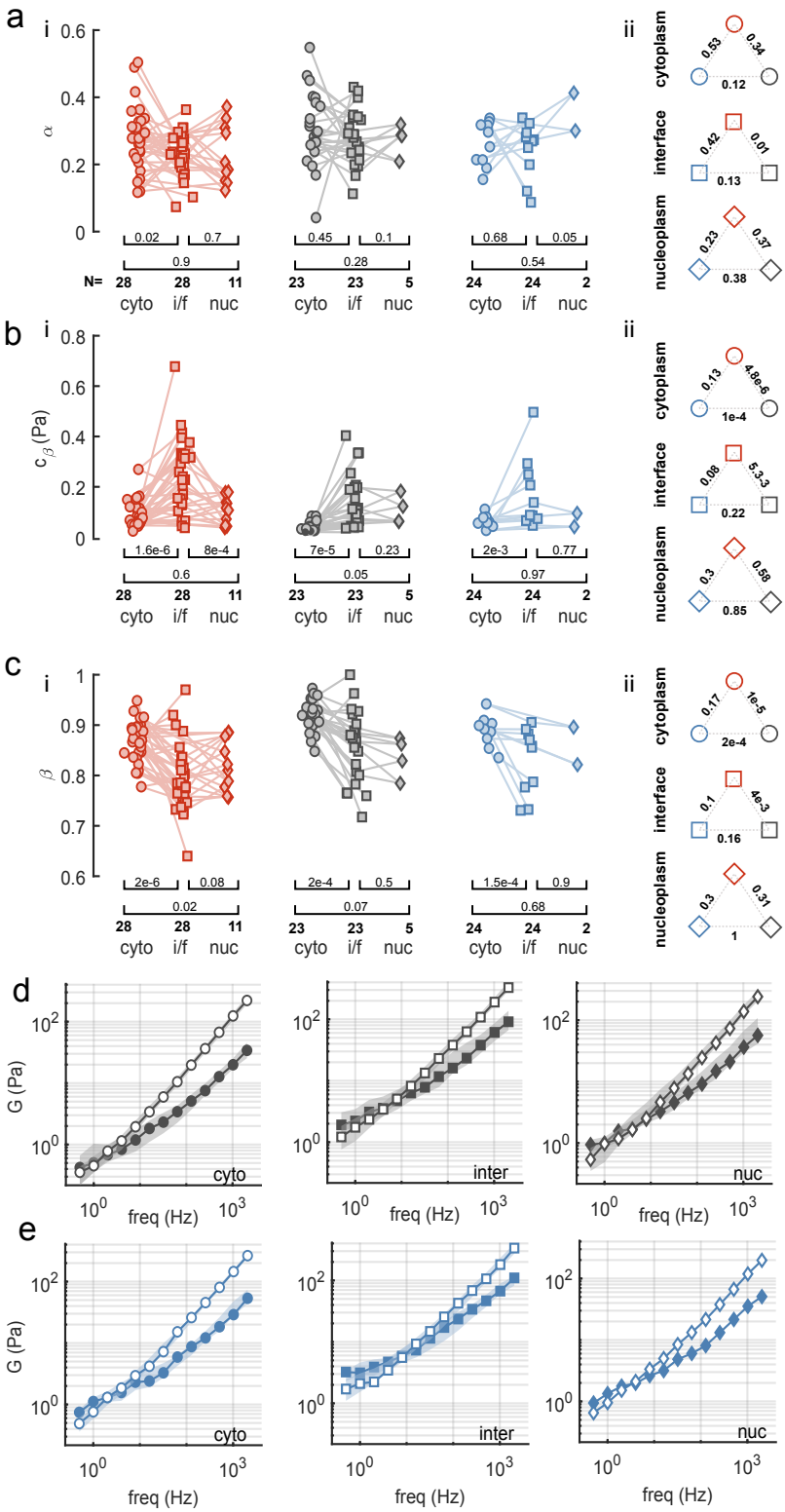
a
i
ii
α
0.6
0.4
0.2
0
0.02
0.7
0.9
0.45
0.1
0.28
0.68
0.05
0.54
N=
28
28
11
23
23
5
24
24
2
cyto
i/f
nuc
cytoplasm
interface
nucleoplasm
0.53
0.34
0.12
0.42
0.01
0.13
0.23
0.37
0.38
b
c_β (Pa)
0.8
0.6
0.4
0.2
0
1.6e-6
8e-4
0.6
7e-5
0.23
0.05
2e-3
0.77
0.97
0.13
4.8e-6
1e-4
0.08
5.3e-3
0.22
0.3
0.58
0.85
c
β
1
0.9
0.8
0.7
0.6
2e-6
0.08
0.02
2e-4
0.5
0.07
1.5e-4
0.9
0.68
0.17
1e-5
2e-4
0.1
4e-3
0.16
0.3
0.31
1
d
G (Pa)
10^2
10^0
10^3
freq (Hz)
cyto
inter
nuc
e

Supp. Data Fig. 4 *(preceding page).* Active microrheology of zebrafish progenitor cells a, (i) Exponent α of the low-frequency component derived from the fit of the fractional Kelvin-Voigt to the rheological spectrum in Fig 4. p-values below the graph derived from a paired t-test; N=number of cells measured. (ii) p-values derived from a pairwise, tow-sided Mann-Whitney U-test of the indicated combinations. **b,** (i) Prefactor c_β of the high-frequency component derived from the fit of the fractional Kelvin-Voigt to the rheological spectrum in Fig 4. p-values below the graph derived from a paired t-test; N=number of cells measured. (ii) p-values derived from a pairwise, tow-sided Mann-Whitney U-test of the indicated combinations. **c,** (i) Exponent β of the high-frequency component derived from the fit of the fractional Kelvin-Voigt to the rheological spectrum in Fig 4. p-values below the graph derived from a paired t-test; N=number of cells measured. (ii) p-values derived from a pairwise, tow-sided Mann-Whitney U-test of the indicated combinations. **d, e,** Rheological spectrum derived from (d) latrunculin A treated cells and (e) Lamin A overexpressing cells

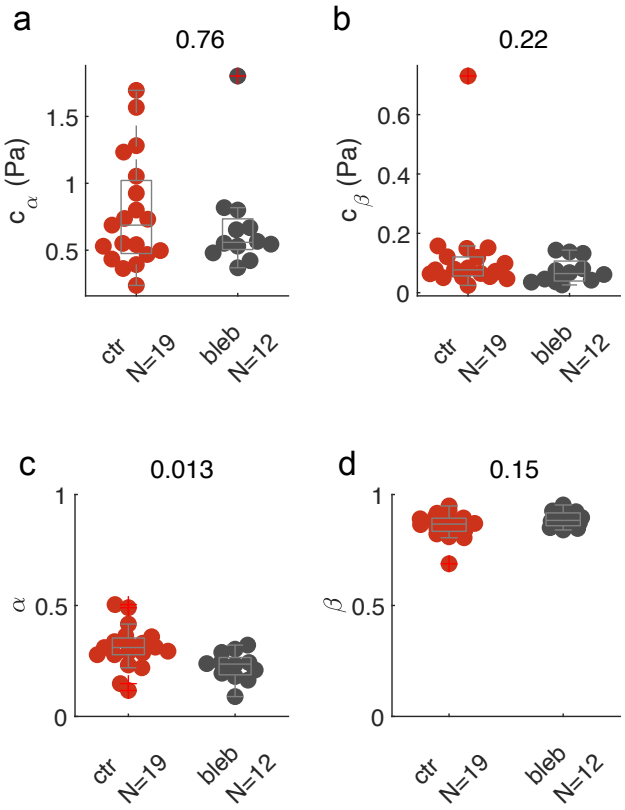

Supp. Data Fig. 5. Cytoplasmic rheology is unaffected by myosin II activity. Dot plot of all four parameters extracted from a fit of the rheological spectrum to a fractional Kelvin-Voigt model comparing the cytoplasm of untreated control cells with cell treated with 10 μM blebbistatin. **a,** Prefactor c_α indicating magnitude of the low-frequency, elastic response; **b,** Prefactor c_β indicating magnitude of the high-frequency, viscous response; **c,** Exponent α indicating the low-frequency, solid behavior; **d,** Exponent β indicating the high-frequency, fluid behavior. Values above the plot indicate the p-value of an unpaired t-test.

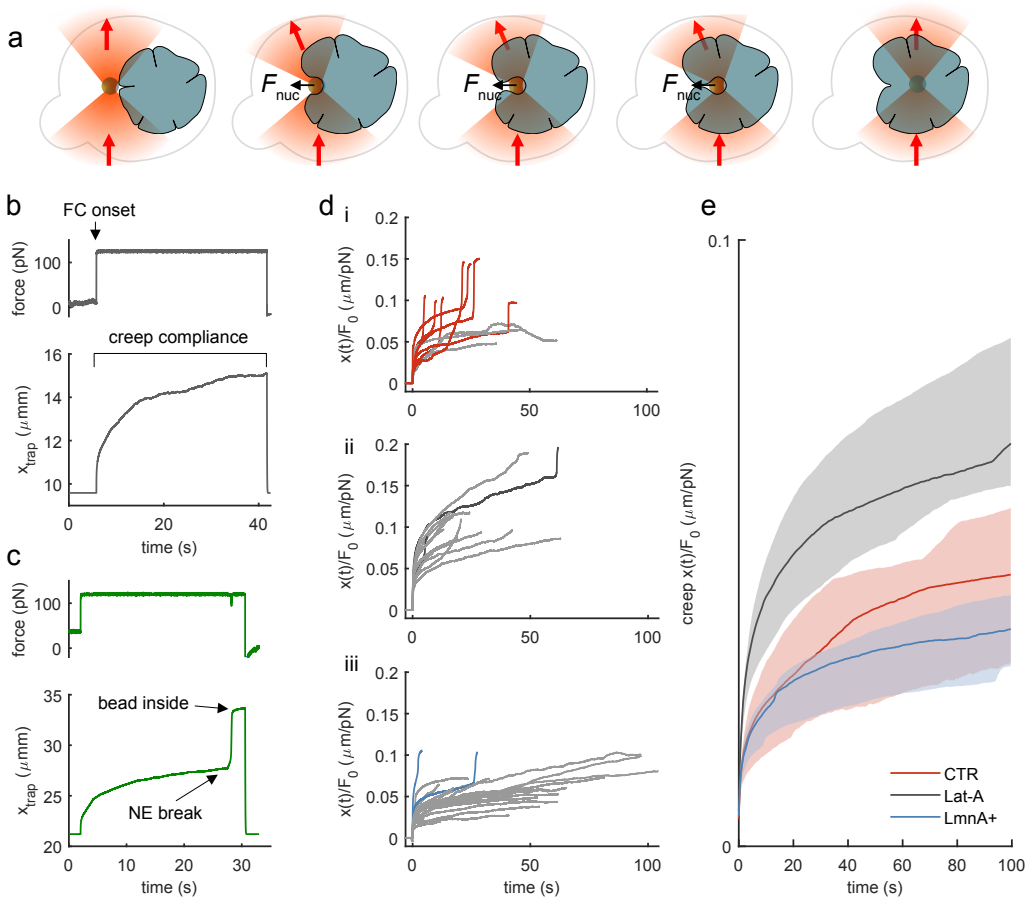

Supp. Data Fig. 6. Force clamp protocol for microsphere insertion of into zebrafish embryonic cell nuclei. a, Schematics of the nuclear insertion process using the force clamp modality of the optical micromanipulation platform. A bead is brought into contact with the nucleus and a force clamp is set at $F_0 \sim 100 - 150$ pN. During some tens of seconds, the bead creeps against the nuclear envelope, eventually breaking it and entering the nucleus. **b,** Example of an unsuccessful bead insertion assay. The nuclear envelope is too stiff for the optical trap to break it. At $t \sim 5$ s, the force is set to 120 pN (top) and the trap pushes the bead against the nucleus. After $t \sim 40$ s, the force clamp is turned off. **c,** Example of a successful insertion. Similar to B, a force clamp of $F_0 = 120$ pN is initiated at $t \sim 5$ s. Around $t \sim 25$ s, the nuclear envelope breaks and the trap accelerates into the nucleus. After this, the force clamp is turned off. **d,** Summary for control cells (i), cells incubated with latrunculin A (ii) and cells with lamin A overexpression (iii). Trajectories have been normalized with respect to the force setpoint as $x(t)/F_0$. Colored traces (red: CTR; black: Lat-A; blue: LmnA+) indicate successful events in which the bead gets inserted into the nucleus. Gray lines are force compliance curves that didn't succeed in inserting the bead into the nucleus. **e,** Normalized creep trajectories over the first 5 seconds of creep test. Solid lines are medians and shaded areas correspond to the $\pm 25\%$ quantiles.

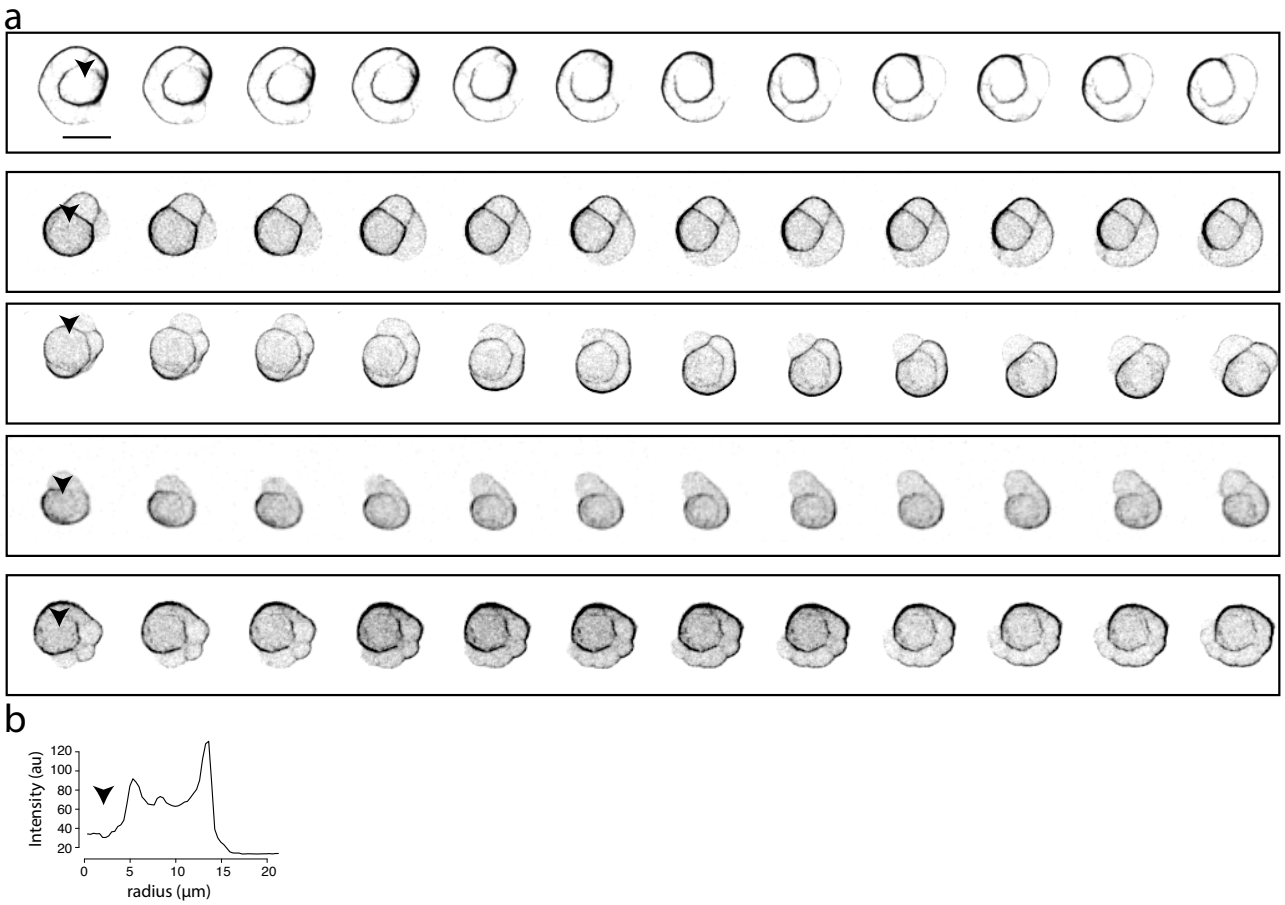

Supp. Data Fig. 7. Actin distribution in isolated progenitor cells undergoing blebbing behavior a, Montage of five different isolated mesendoderm progenitor cells, showing dynamics of filamentous actin stained with lifeact-GFP. Arrowhead indicates the location where the nucleus is expected. Note, how the 'old' cortex collapses onto the cell center and accumulates around the nucleus. Length of each sequence, t=120s. Scalebar=10µm. Cells were injected with 50pg lifeact-GFP to visualize filamentous actin and were isolated in sphere/dome stage according to the methods described in this manuscript. Data set from ref. [48]. **b,** Radial profile plot of the averaged intensity as a distance from the cell center. Arrowhead points to the nuclear location.

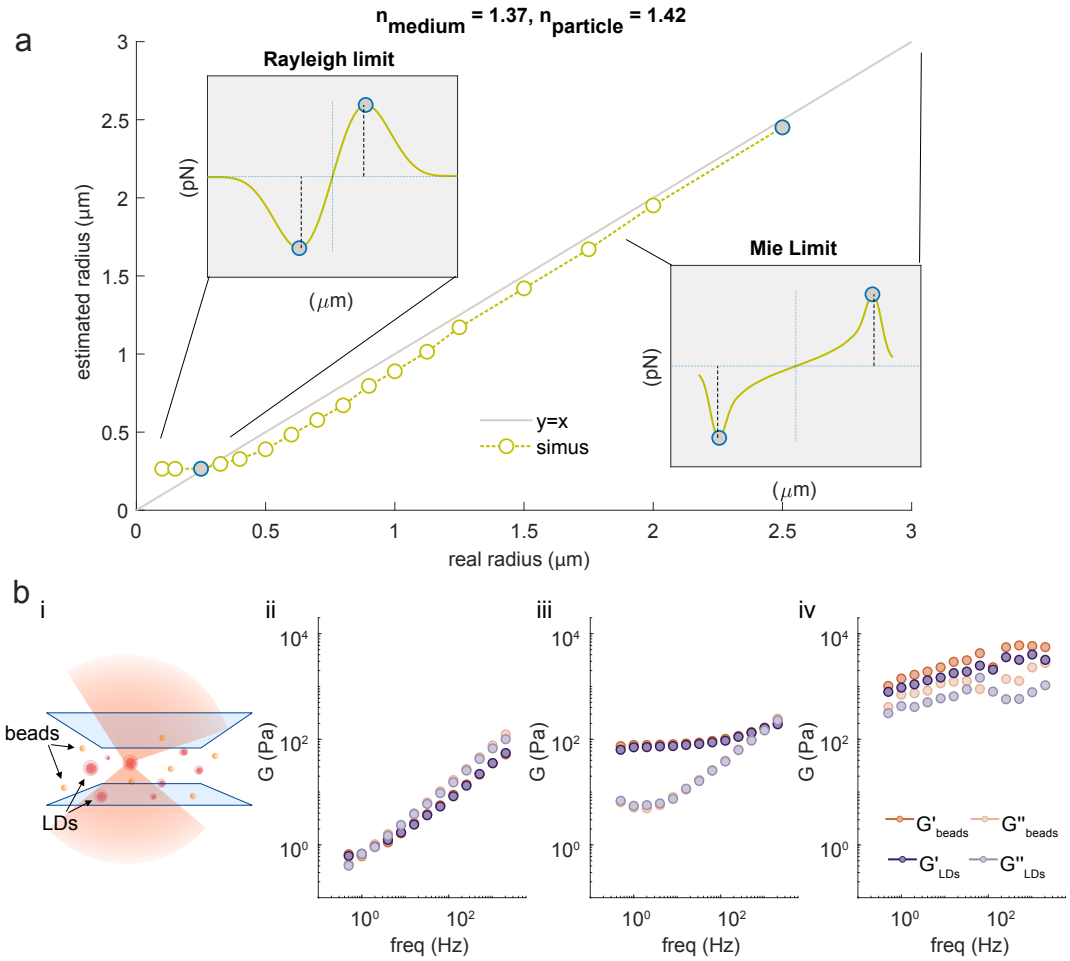

Supp. Data Fig. 8. Lipid droplets correctly measure rheological properties up to several kPa.
a, Estimation of the LD size using simulations with the Optical Tweezers Toolbox [57]. The refractive index of the lipid droplet was considered $n_{\mathrm{LD}} = 1.42$ and that of the tissue $n_{\mathrm{worm}} = 1.37$. The numerical aperture of the laser trapping beam was approximated to 1 as the entrance pupil of our NA=1.2 trapping objective is underfilled with a factor of 0.8. We considered radii from $R = 0.1$ µm to $R = 2.5$ µm. From the force profiles, we could measure the peak-to-peak radius, and finally obtained a look-up table from which the *real radius* is obtained from the *estimated radius* from the force scan across the LD. Insets i and ii show examples in the Rayleigh and Mie regimes, respectively. While the radius of probes in the strict Rayleigh regime degenerates and can't be addressed, the estimated radius tends to the real radius in the Mie regime (geometrical optics). **b,** (i) Schematic of the experiment. Lipid droplets are isolated from *C. elegans* and embedded into a poly-acrylamide gel with varying crosslinker (bis-acrylamide) concentration. (ii-iv) Comparison of the rheological spectrum performed with the lipid droplets and the polystyrene microspheres, embedded into a gel with ii) 2-10 Pa, iii) 10-100 and iv) 100-1000 Pa elastic modulus.

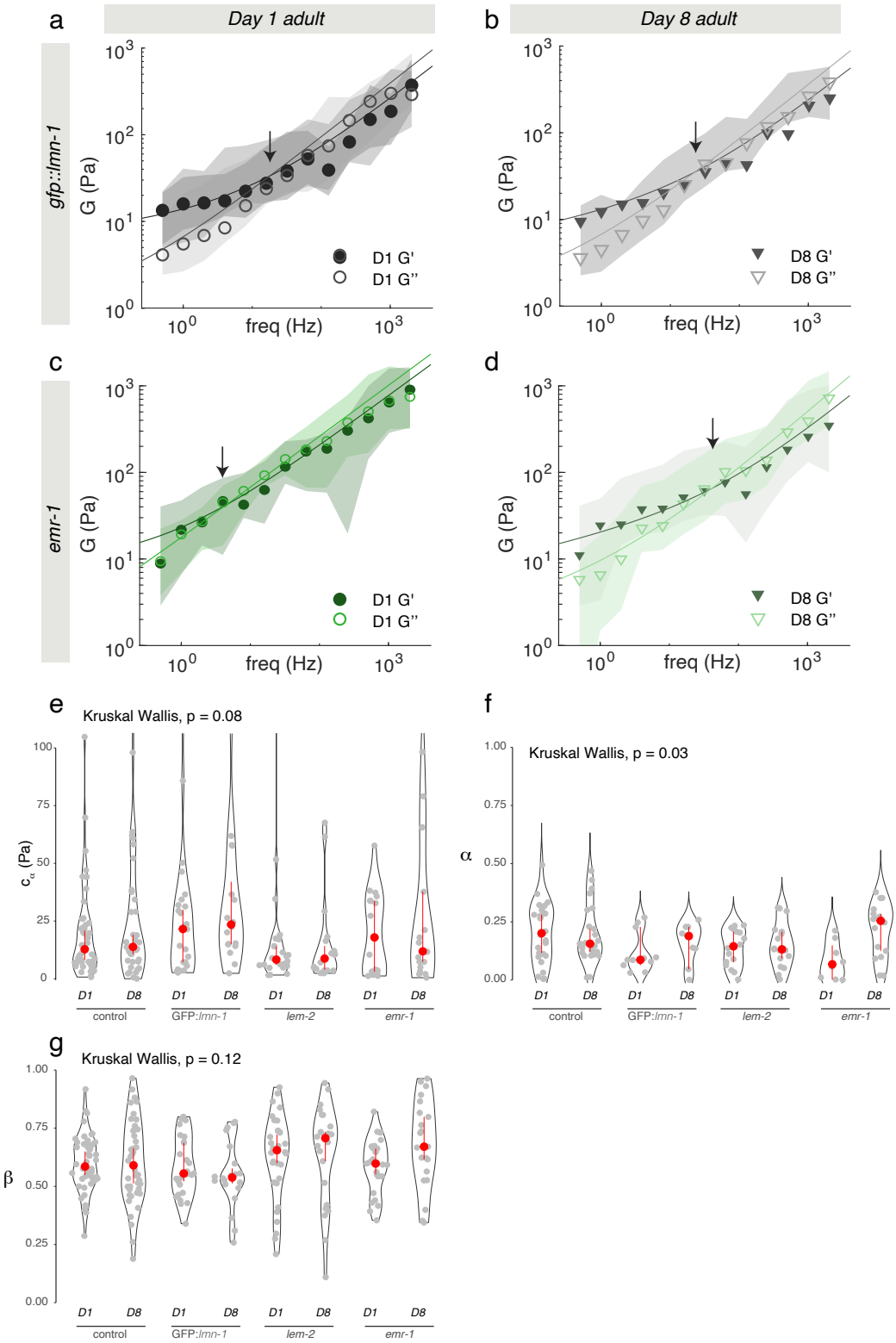
a
Day 1 adult
b
Day 8 adult
gfp::lmn-1
G (Pa)
freq (Hz)
D1 G'
D1 G''
D8 G'
D8 G''
c
d
emr-1
e
Kruskal Wallis, p = 0.08
c_α (Pa)
f
Kruskal Wallis, p = 0.03
α
g
Kruskal Wallis, p = 0.12
β
D1
D8
control
GFP:lmn-1
lem-2
emr-1

Supp. Data Fig. 9 *(preceding page).* Mutations in nuclear envelope sensitize the cytoplasm of *C. elegans* to age-related changes in viscoelasticity.
a, b, Rheological spectrum derived from dominant-negative *gfp:lmn-1* expressing animals at (a) day 1 and (b) day 8 adulthood. **c, d,** Rheological spectrum derived from *emr-1* mutant animals at (a) day 1 and (b) day 8 adulthood.The median and $\pm$25%quantiles are represented by lines and shadows, respectively. **e,** Prefactor c_α of the low-frequency component derived from the fit of the fractional Kelvin-Voigt model to the rheological spectrum in Fig 5e,f and panels a-c above. **f,** Exponent α of the low-frequency component derived from the fit of the fractional Kelvin-Voigt model to the frequency spectrum. **g,** Exponent β of the high-frequency component derived from the fit of the fractional Kelvin-Voigt model to the frequency spectrum. Red circle indicates median$\pm$bootstrapped 95% confidence interval. For statistical comparison and p-values see Supplementary Table 2.

5 Materials and Methods

5.1 Theory and simulation of the trap displacement in a viscoelastic medium in a time varying trapping potential

The effect of having two alternating optical traps on the actual measurement of the response function, $\chi(\omega)$, and thereby the G modulus, $G(\omega)$, is introduced in this section and detailed in the Supplementary Information. Two methods are introduced. First, we use a numerical method in the time domain, aiming at the trajectory of the trapped probe, in order to emulate the violation of the continuity condition between the force $F_T(t) = F_1(t) + F_2(t)$ and position $x_p = F_2/k$ measurements (Figs. 1 and 2). Second, by truncating the dynamic, oscillatory trapping potential at the first harmonic, we obtain an analytical expression in the frequency domain that we further use to compensate the time-sharing effect.

Study of the deviation via Fractional Differential Equations

Under an AOD-modulated time-sharing regime, the laser spot gradually vanishes from trap 1 and appears into trap 2 as the acoustic wave enters the laser beam cross section at the AOD crystal (see Supplementary Information). In our set-up, this occurs within a transition time of $\tau = 10$ µs. After that, the laser spot remains at trap 2 for 30 µs and the transition is thereby reversed back into trap 1. Meanwhile, a voltage datum is sampled with a delay of 33 µs with respect to the rising edge of the acoustic wave. Because traps 1 and 2 fall within the linear regime of the trapped particle, forces acting onto it are equivalent to that from a single trap undergoing the following trapezoidal trajectory (see Supplementary Information):

$$x_{l,n}(t) = \begin{cases} x_{2,n} - \frac{t}{\tau}(x_{2,n} - x_{1,n}) & 0 \leq t < 10 \text{ µs} \\ x_{1,n} & 10 \text{ µs} \leq t < 40 \text{ µs} \\ x_{1,n} - \frac{t}{\tau}(x_{1,n} - x_{2,n}) & 40 \text{ µs} \leq t < 50 \text{ µs} \\ x_{2,n} & 50 \text{ µs} \leq t < 80 \text{ µs} \end{cases} \qquad n = 0, 1, 2, ... \tag{2}$$

where $x_{2,n} = 0, \forall n$ and $x_{1,n}$ are discrete values of $x_1(t) = 2x\sin(\omega t)$ sampled at $f_t = 12.5$ Hz. Here, the amplitude of the oscillation in $x_1(t)$ is expressed as $2x$ for convenience. In order to capture the power law rheological behavior of most samples in biology, we use the fractional time-derivative operator, D_t^α, which describes the stress-strain relationship of a springpot, $\sigma(t) = c_\alpha D_t^\alpha \epsilon(t)$ [34]. This element represents, continuously, all viscoelastic responses between the purely elastic unit —the *spring*, with

$\sigma(t) = \kappa\epsilon(t)$— and the purely viscous unit —the *dashpot*, with $\sigma(t) = \gamma \frac{d}{dt}\epsilon(t)$. We numerically solved the equations detailed in Table 1 to obtain the trajectory of the probe bead, $x(t)$, at different driving frequencies, ω_j. The instantaneous force is thereby obtained as $F(t) = k(x_l(t) - x(t))$, from which the interleaved BFP interferometry voltage signals, $V_1(t_{1,i})$ and $V_2(t_{1,i})$, are sampled at time points $t_{1,i}$ and $t_{2,i}$, respectively. Finally, the fast Fourier transform of the two signals is taken and the response function, $\hat{\chi}_t(\omega_j)$, and G modulus, $\hat{G}_t(\omega_j)$, obtained using Eqs. 1. We developed a package in Python to carry out the FDE simulations (see more details in the Suppl. Information). The comparison between the physical response function, $\hat{\chi}(\omega_j)$, and the one accounting for the time-sharing deviation, $\hat{\chi}_t(\omega_j)$, is shown in Fig. 2d for three different power-law materials. The corresponding G moduli (both the physical and the time-sharing deviated) are shown Supp. Data Fig. 1.

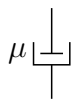

$$(6\pi r) \cdot \mu D_t^1 x(t) = k\left[x_l(t) - x(t)\right] \tag{3}$$

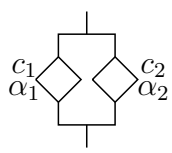

$$(6\pi r) \cdot \left[c_1\, D_t^{\alpha_1} + c_2\, D_t^{\alpha_2}\right] x(t) \;=\; k\left[x_l(t) - x(t)\right], \tag{4}$$

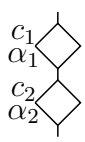

$$\begin{aligned} (6\pi r) \cdot c_1 D_t^{\alpha_1} x_1(t) &= k\left(x_l(t) - x(t)\right), \\ (6\pi r) \cdot c_2 D_t^{\alpha_2} x_2(t) &= k\left(x_l(t) - x(t)\right), \\ x(t) &= x_1(t) + x_2(t) \end{aligned} \tag{5}$$

Table 1. Fractional-differential equations for a purely viscous dashpot (top), fractional Kelvin-Voigt (middle) and fractional Maxwell (bottom) models.

5.2 The First Harmonic Approximation (FHA)

The second approach to the study of deviation is based on analytically solving the equations of motion of the bead $\hat{x}(\omega')$ in the space of frequencies ω'. The equation to be solved is the algebraic equation

$$\hat{x}(\omega') = \hat{\chi}(\omega')\, k\left[\hat{x}_l(\omega') - \hat{x}(\omega')\right], \tag{6}$$

which becomes

$$\hat{x}(\omega') = \hat{\chi}_a(\omega')\, k\, \hat{x}_l(\omega'), \tag{7}$$

Here, $\hat{\chi}_a(\omega')$ is the the response function of the active-passive system (see Supplementary Materials). $\hat{x}_l(\omega')$ is the Fourier transform (FT) of the First Harmonic Approximation (FHA) of the trap trajectory, which in the time domain t reads:

$$x_l(t) = \frac{x_1}{2} \exp(i\omega t)[1 + \sin(\omega_t \cdot t)], \tag{8}$$

where the complex oscillation $\exp(i\omega t)$ is used, instead of a real one such as $\sin(\omega t)$ or $\cos(\omega t)$, with the sole purpose of simplifying the notation in the frequency space. After FT, the trap trajectory reads

$$\hat{x}_l(\omega') = \frac{x_1}{2} \left[\delta(\omega' - \omega) + \frac{\delta(\omega' - \omega_+) - \delta(\omega' + \omega_-)}{2\, i} \right], \tag{9}$$

with $\omega_\pm = \omega_t \pm \omega$ and where $\delta(\omega')$ is the Dirac distribution.

To get the linear response function $\chi_t(\omega)$ from the FHA approximation, the same steps identified for the FDE simulation must be followed, but this time using an analytical approach. The details of the calculations are given in the Supplementary Material. The obtained expression of $\hat{\chi}_t(\omega)$ is a function of the response function of the material $\hat{\chi}$, of the time sharing frequency ω_t, of the trap stiffness k and reads

$$\hat{\chi}_t(\omega) \;=\; g\left(\hat{\chi}, \omega_t, k\right)(\omega) = \frac{\hat{\chi}(\omega) - \hat{\chi}_1(\omega) + k\left[\hat{\chi}(\omega)\hat{\chi}_1(\omega) - \hat{\chi}_+(\omega)\hat{\chi}_-^*(\omega)\right]}{1 + 2\,k\hat{\chi}_1(\omega) + k^2\hat{\chi}_+(\omega)\hat{\chi}_-^*(\omega)}, \tag{10}$$

where

$$\hat{\chi}_1(\omega) = \frac{1}{2}\left[\hat{\chi}_+(\omega) + \hat{\chi}_-^*(\omega)\right] \tag{11a}$$

$$\hat{\chi}_+(\omega) = \hat{\chi}(\omega_t + \omega) \tag{11b}$$

$$\hat{\chi}_-^*(\omega) = \hat{\chi}^*(\omega_t - \omega) = \hat{\chi}(-\omega_t + \omega), \tag{11c}$$

and the asterisk * denotes the complex conjugate operation.

The results of the Eqs. 10 and 11 show that $\hat{\chi}_t(\omega)$ depends on the response function $\hat{\chi}$ measured at different frequencies. In addition to the contribution at the excitation frequency ω, the contributions from

the sidebands of the amplitude-modulated signal at the frequencies $\omega_- = \omega_t - \omega$ and $\omega_+ = \omega_t + \omega$ also determine the behavior of $\hat{\chi}_t(\omega)$.

Before using Eq. 10 to understand the causes of the deviation, the goodness of the FHA approximation should be checked by comparing the results predicted using Eq. 10 with those predicted using the FDE approach. To do so, we applied the FHA correction to the deviated data simulated through FDE 2d.

5.3 Optical micromanipulation and fluorescence microscopy

Optical tweezers

Our optical micromanipulation and microscopy platform is built around an inverted microscope (Nikon Ti-2) and has been used in previous publications and described extensively elsewhere [29]. A commercially available optical tweezers unit (SENSOCELL, Impetux Optics) is coupled to the rear epi-fluorescence port of an inverted Ti2 Nikon microscope. The trapping laser is modulated by a pair of acousto-optic deflectors (AODs) optically-conjugated to the entrance pupil of a water-immersion objective (Nikon Plan Apo, 60x NA=1.2), which in turn focuses the trapping beam onto the focal plane thus generating the optical traps. A direct force sensor substituting the bright-field illumination condenser captures the light from the optical traps, that has interacted with the sample, to detect transverse light momentum changes without the need for *in situ* optical trap calibration[24]. Between the trapping objective and the optical force sensor, samples are mounted with two glasses as detailed below for each type of experiment.

Force and position detection with time-sharing optical tweezers

Optical force measurements were carried out through capture of trapping light momentum changes, which enables measurement of trapping forces on irregular samples, as well as in non-viscous media, with a sample-independent calibration [24, 65]. Briefly, light captured with a BFP interferometry system, optimized for light momentum detection (SENSOCELL, Impetux Optics), is conveyed to a position-sensitive detector (PSD), which volt-to-pN conversion factor, α, is calibrated by the manufacturer. The same system can be used to measure probe positions —relative to the trap—, after calibration of the trapping stiffness, k (pN/μm), which is performed by fast scanning the trap across the probe. Variations

in the initial light momentum and trap power over the field of view are compensated through the driving software of the optical traps (LightAce, Impetux Optics). A detailed protocol for the start-up and use of this optical tweezers platform can be found elsewhere [29].

Active microrheology

Our active microrheology measurements consist of four steps:

- Measuring the initial light momentum variation around the trapped probe. *Needed for solid samples that require trap/probe centering.*
- Measure the trap stiffness.
- Apply a series of oscillations with specific parameters of frequency, amplitude and measurement duration. The frequencies and amplitudes applied in every measurement are specified in Supplementary Tables S1-4
- Retrieval of the $\hat{\chi}_t(\omega)$ and $G(\omega)$ values through the First Harmonic Approximation method.

The experimental scheme detailed in Section 5.1 is implemented using the manufacturer's AOD-addressing software (LightAce, Impetux Optics) and analysed through an executable interface (Rheo-Analysis, Impetux Optics), which includes the TimSOM compensation pipeline, $\hat{chi}_t \rightarrow \hat{\chi}$ thoroughly described in the Supplementary Text file.

Spinning-disk confocal microscopy

A multimodal spinning-disk confocal unit (Andor Dragonfly 505, Oxford Instruments) is coupled to the left port of the microscope. It is composed of seven excitation lasers stabilized through a wavefront filter (Borealis, Oxford Instruments) and the corresponding dichroic optics for multiple beam combinations. For GFP and mCherry parallel imaging, the 488 nm and 561 nm laser wavelengths were chosen, were directed to the sample through a quad-band dichroic mirror (405 nm, 488 nm, 561 nm, 640 nm) and a spinning disk with an array of 40 µm diameter pinholes rotating at 6000 rpm. The fluorescence emission signal was collected by the same objective, sent back to the confocal unit and directed to the cameras

through the dichroic mirror. A long-pass dichroic mirror (cutoff wavelength: 565 nm) split the red and green signals, which were respectively imaged by two sCMOS cameras (Andor Sona, Oxford Instruments). For DAPI and GFP parallel imaging, the 405 nm and 488 nm laser wavelengths and the same quad-band dichroic mirror were chosen. Fluorescence emission was further split with a 500 nm cutoff wavelength long-pass dichroic mirror.

Microrheology in calibrated materials

Glycerol solutions Different concentrations of glycerol mixed with fluorescent bead solution (1 µm, Carboxylate-Modified microspheres, Thermofisher) were prepared to calibrate the TimSOM technique in a viscous material. The concentrations ranged from 0% (MilliQ water) to 95% glycerol and were prepared gently avoiding the formation of bubbles from a 99% glycerol stock solution. Since the material is purely viscous, the trapped microsphere will relax into the trap focus, ensuring alignment with no need of a probe/trap centering routine (see below). We obtained the viscosity, η_{TimSOM}, for the glycerol mixtures from the slope of the loss modulus $G''(\omega) = \eta_{TimSOM}\omega$ (Supp. Data 2b).

To benchmark the results, we performed Stokes-drag force measurements, on the same bead, after the time-sharing microrheology routine. We applied triangular waveforms with increasing velocities, v_{trap}, until the microsphere escaped the optical trap (Supp. Data Fig. 2a). The plateau force during the bead movement, F_{drag}, increased with velocity, indicative for a purely viscous liquid. We then estimated the viscosity, η_{drag}, by fitting $F_{\text{drag}}(v_{\text{trap}}) = (6\pi\eta_{\text{drag}}Rv_{\text{trap}})$ to the force-velocity plots, where R is the radius of the trapped microsphere (Supp. Data Figure 2a ii). To avoid changes in viscosity due to laser absorption, trapping power was left below P =65 mW [83]. To avoid hydrodynamic interaction with the chamber surfaces, the trapping plane was kept at a relative height of $z = 20$ µm [84].

Polyacrylamide gels Soft PAA gels were polymerized from a modification to the recipe used in [85]. A gel premix (GPM) made of 30% acrylamide (Sigma A8887) and 0.8% bisacrylamide solution (Sigma 66670) is mixed with 5µL of fluorescent microsphere solution at stock concentration (2% solids, F8816, Thermofisher) and diluted in water or a solution of isolated lipid droplets for lipid droplet characterization (Supp. Data Fig. 8). Exact quantities for obtaining specific gel stiffness are tabulated in 2. GPM

containing microspheres was thoroughly resuspended and later mixed with 5 µL of amonium persulfate (APS, Sigma A3678, 10% diluted in PBS) and 1.5 µL TEMED (Sigma T9281) for the polymerization process. Prior to gelling, 40 µL of the solution were transferred into the optical trapping cavity. The cavity was then closed with a #1.5 cover glass as described above[29]. Measurements were performed after 30 minutes of the sample preparation in order to have the gel homogeneously polymerized.

Because the gels are a viscoelastic solid material, in general, the embedded probe will not relax into the center of the optical trap once it is placed on it. A probe/trap centering routine, followed by the trap stiffness calibration, was therefore carried out before the microrheology measurement over the frequency series.

estimated stiffness	Acryl-Bisacryl	Water	TMED	APS	Beads
1-10 Pa	41	540	1.5	5	5
10-100 Pa	46	535	1.5	5	5
100-1000 Pa	55-65	526-516	1.5	5	5

Table 2. Reagents for PAA Gels of different stiffness. All quantities are in microliters

Creep Compliance measurements An independent measurement of the G modulus of polyacrylamide gel was obtained through measurement of the creep compliance upon the application of a step in stress, using LightAce's force clamp utility at a given setpoint force. We used a trap stiffness of 890pN /μm and 220μN/μm for stiff and soft gels respectively. To do so, we set the proportional gain to Kp=0.001 , 0.004μm/ pN, the integral gain to Ki=1.1, 4.5 μm/ pN. s and the derivative gain to Kd=0 for a stiff and a soft gel respectively. With these parameters we set a constant force of $F_0 = 40$ pN, which leads to a typical viscoelastic compliance curve, $x(t)$. We thereby used the mathematical model derived by Evans et al. [35], implemented in custom Matlab code, to calculate the frequency-dependent shear modulus from measurements of $J(t)$ in the time domain. For two gels with different stiffness, results are plotted in Supp. Data Fig. 2c, d. The position of the trapped probe was calculated as $x_{\mathrm{bead}} = x_{\mathrm{trap}} - F/k_{\mathrm{OT}}$. The low-frequency plateau modulus was calculated from the frequency-dependent storage G-modulus after fitting to a fractional Kelvin Voigt model and indicated in the Supp. Data Fig. 2c, d.

PDMS Poly-dimethyl-siloxane prepolymer was mixed with a curing agent at 100:1 and mixed thoroughly with 1 µm microspheres (F8816, Thermofisher). The solution was degassed in a vacuum pump to eliminate bubbles introduced during the mixing. The mixture was used immediately for rheology to avoid long-term curation of the silicone. Due to the high viscosity of the solution, the bead did not relax into the trap in a time short enough for experiment viability, hence the probe/trap centering routine was used.

Zebrafish experiments

Husbandry

Wild-type embryos were obtained from the AB strain background and actin was visualized with a stable transgenic line (Tg(actb2:Lifeact-GFP)) [86]. Zebrafish embryos were kept in E3 medium at 25° to 31 °C before experiments and their stages were identified according to hours post-fertilization (hpf) and morphological criteria [87]. All protocols used have been approved by the Institutional Animal Care and Use Ethic Committee (PRBB–IACUEC) and implemented according to national and European regulations. All experiments were carried out in accordance with the principles of the 3Rs (replacement, reduction, and refinement).

Microsphere injection and cell preparation

Zebrafish embryos were injected 1 nL of microspheres (F8816, Thermofisher) at 1:5 of the stock solution at the one-cell zygote stage in order to ensure proper distribution of microspheres, as described elsewhere [29]. When the embryos reached sphere stage (approximately at 4 hpf), they were dechorionated with a pair of forceps and their cells were manually dissociated and left for at least 30 min to recover[88]. A layer of double scotch tape (approximately 20 x 20 mm wide) was used as a spacer between the lower and the upper surfaces. A 1x1 cm hole was made and the layer was adhered onto the bottom dish (GWST-5040, Willco). After incubation with concanavalin A to promote cell adhesion ($t = 30$ min, 100 µL, 0.5 mg/mL, C5275 Sigma,[89]), cells were plated onto the bottom dish surface and the cavity was covered at the top with a 22x22 cm cover glass (Ted Pella).

The following are the mRNAs were synthesized *in vitro* using the mMessage mMachine Kit SP6

Kit(Ambion AM1340M). They were injected at the one-cell stage together with the microspheres :

- Lap2B-GFP[7] (inner nuclear membrane visualization) 80pg per embryo
- GPI-GFP (plasma membrane visualization, we thank Michael Brand for the pCS2 + GPI-GFP plasmid) 50pg per embryo
- RFP-lamin-A (LaminA overexpression, this study) 100pg per embryo
- NLS-GFP (soluble nuclear marker), 100 pg per embryo

5.4 Plasmid cloning for mRNA injection

To clone LaminA (ENSDARG00000013415) we used cDNA previously retrotranscribed (Xpert cDNA Synthesis kit GK80.0100, Grispr) from total mRNA isolated using 24 hpf zebrafish embryos (TripleX-tractor direct RNA GK23.0100, Grispr). To generate the RFP-LaminA fusion protein and clone it into a vector, Phusion HF (Thermofisher F530S) was used to amplify both fragments for LaminA and RFP with the primers listed in SuppTable6

The Gibson Assembly System (in-house production) was used to introduce both fragments into a pCS2 vector previously digested and linearized with EcoRI/XbaI. pCS2 LaminA-RFP was linearized with the NotI enzyme (NEB R3189S) and used as a template to synthesize mRNA using the mMessage mMachine SP6 kit (Ambion, AM1340M).

Active microrheology measurements in zebrafish progenitor stem cells

Details of the trapping experiments and microsphere selection are described in reference [29]. To perform active microrheology measurements inside a cell, first, a cell with one or two microspheres in the cytoplasm is selected. Then, a working optical plane is identified looking at nucleus fluorescence, where the nucleus has its biggest cross-section. Subsequently, the microsphere is trapped and placed in the selected plane between the plasma and nuclear membrane, avoiding adhesions to either one. After placement, the active microrheology, with parameters shown in SuppFigure 7, is initialized.

After the measurement of the cytoplasm is completed, to get the measurement in the cytoplasm-nucleus interface, the bead is placed to be in contact with the nuclear envelope. This is done by slowly moving the microsphere toward the nucleus and following the force signal. When the microsphere touches the NE there is a peak of force followed by an exponential relaxation after the bead stops moving. In this position, the microrheology routine is once again started, this time with the oscillations being perpendicular to the NE. Finally, after the bead is inserted in the nucleus with the protocol described in the following section, the same routine is performed with the microsphere trapped inside the nucleus. The oscillations of this measurement are done perpendicular to the insertion direction. All active microrheology measurements are performed using a trap power of 60mW to 100mW at the sample.

Microsphere insertion into the nucleus

The process of inserting the microsphere inside the cell nucleus consists of applying a routine in which the force applied by the optical trap is clamped using the optical force feedback system explained above (Force set-point $F = 100 - 150$ pN). In this way, the force applied is constant and what is changing is the trap position and thus the microsphere position. First, the bead is placed in contact with the nucleus at the optical plane where its fluorescent cross section is the biggest. Then the clamp is set from 100pN to 150pN and it is activated until the bead is inserted, or until the microsphere does not indent more or gets lost.

Experiments in *C. elegans*

C. elegans maintenance

Strains were maintained and manipulated under standard conditions [90]. Nematode strains were grown at 20°C on nematode growth medium (NGM) plates with OP50 bacteria and, synchronized using the standard alkaline hypochlorite treatment method [91]. Only age-matched, synchronized adult hermaphrodites were used in this study.

C. elegans transgenesis

Nematode strains used in this study are described in SuppTable 6. MSB1136 was generated in two steps. First, *sfGFP11* ssODN sequence (Table 2) was endogenously inserted at the N-terminus of lmn-1 locus by HDR (homology-directed repair) using CRISPR-Cas9 technology and following a co-CRISPR strategy using *dpy-10* as a marker to enrich for genome-editing events [92, 93, 94, 95]. Thus, obtaining MSB1126. Guide RNA (SuppTable 7) was designed using both Benchling (www.benchling.com) and CCTop [96] online tools. Second, MSB1126 was crossed to CF4588 [97] (TABLE 1) provided by CGC, finally obtaining MSB1136 (TABLE 1). MSB1136 shows high expression LMN-1::sfGFP signal in somatic cells and does not present any phenotype in terms of development and lifespan compared to the reference wildtype strain N2, thus considering MSB1136 as a wildtype-like strain.

Lipid droplet isolation

C. elegans lipid droplets isolation was performed following the protocol previously described [54] with minor modifications. Briefly, for sample preparation, MSB1136 animals were grown on peptone-enriched plates seeded with NA2 bacteria and, synchronized using the standard alkaline hypochlorite treatment method [91]. 2 x 10^4 synchronized larva 1-stage nematodes were plated and grew at 20°C until either day 1 or day 8 adulthood for sample collection. For lipid droplets day 8 collection, animals were washed off with M9 and separated from laid eggs by gravity, to avoid generation mixing, before transfer to new plates. On the day of the experiment, plates were washed off, and animals were collected using PBS. After washing the sample three times with buffer A [54], the pellet was resuspended in the same buffer supplemented with protease inhibitor (Sigma Aldrich, P8340). From now on, the sample was manipulated either on ice or at 4°C. Nematodes homogenization and cell disruption were performed by using an ultrasonic bath (VWR, USC300TH) four times, 1 min per time, with 30-s intervals. Lipid droplets were collected in buffer B [54] from the post-nuclear fraction by ultracentrifugation followed by three washing steps as described in Ding et al. 2013. Isolated lipid droplets were used within the same day for active microrheology routine in polyacrylamide gels (see section above).

814 **Refractive index matching assay**

815 Refractive index of freshly isolated lipid droplets were measured following the standard procedure [98]
816 using the commercially available iodixanol solution (OptiPrep, Sigma Aldrich, D1556) [55]. Lipid
817 droplets solution were gently mixed, accordingly, at different iodixanol concentrations until reaching the
818 matching refractive concentration (48%) and, 0.5% membrane dye BioTracker NIR750 (Sigma Aldrich,
819 SCT113). For lipid droplets' optical trap scanning and imaging, the sample was mounted in optical
820 trapping cavity and then sealed with a 1.5-cover glass, as previously described.

821 **Lipid droplets characterization by TimSOM *in vitro***

822 To prepare PAA gels of different stiffness containing both lipid droplets and microspheres, freshly iso-
823 lated lipid droplets solution was gently mixed with the reagents noted in Table 2. The water was substi-
824 tuted by the same volume of lipid droplet solution for each class of PAA gel. The mix was transferred
825 into the optical trapping cavity and then sealed with a #1.5-cover glass, as previously described. To ex-
826 tract both lipid droplet size and stiffness values measurements were performed alternatively using lipid
827 droplets and microspheres following the procedure detailed above.

828 ***in vivo* TimSOM on *C. elegans* intestinal epithelial cells during ageing**

829 All strains were seeded on NGM plates on the same day and let them grow until day 1 (three days
830 post-seeding) and day 8 (ten days post-seeding) adulthood. For animals evaluated on day 8, they were
831 transferred to new plates every day during the egg-laying period to avoid mixing generations. Because
832 both LW697 and BN20 presented one-day developmental delay compared to MSB1136 and BN19, active
833 microrheology measurements at day 1 and day 8 adulthood for those strains were performed four days
834 and eleven days post-seeding, respectively. The day of the experiment, nematodes were mounted on
835 2% agar pads, immobilized with 10 µM levamisole hydrochloride solution (Sigma Aldrich, 31742), and
836 then covered with a 25 mm-by-25 mm cover glass (Ted Pella, #1.5) sealed with fingernail polish. Active
837 microrheology was performed, as described above for zebrafish progenitor stem cells, on *C. elegans*
838 intestinal cells using endogenous lipid droplets within 1h after immobilization to avoid damage to the
839 animals.

Cuticle curvature evaluation

Cuticles of different age-matched animals were stained with slight modifications as previously described[99]. In short, *C. elegans* strains D1 and D8 were collected and washed using a solution of 0.5% Triton X-100 and M9. Then, animals were incubated in 0.33mg/mL DiI solution (Sigma Aldrich, 42364) for three hours, in agitation and in the dark. Three washes with M9 were made prior to animal mounting, under the same conditions as for TimSOM experiment. For curvature evaluation, Z-scan images were made from different parts of the worm body. From orthogonal sections, the width and height of each portion were measured and width/height ratios were calculated for each condition.

5.5 Protein expression and sample preparation

MEC-2 and UNC-89 SH3 domain proteins were expressed in *E. coli* and purified as described[6]. The sample was prepared in a 10:1 mixture at room temperature.

For dual trap dumbbell microrheology, the surface of the lower coverglass was passivated using this protocol [100]. We used PEG beads ($d = 1$ µm, Micromod, 01-54-103), which were outside the protein condensate and were partially attached to it after short contact [6].

For TimSOM, the coverglass was treated with poly-L-lysine coupled to a polyethyleneglycol group (PLL-PEG, 30 min, 0.5 mg/ml, PLL(20)-g[3.5]-PEG(2), SuSoS). Droplets partially attached to the coverglass, such that the gradient force did not move the floating droplets during the rheology routine. We used carboxy-terminated microspheres that exclusively were found to enter inside the condensates ($d = 1$ µm, Thermofisher, F8816).

5.6 Data analysis

The analysis of the data measured with the active microrheology is performed in RheoAnalysis (IMPETUX). In this program, the complex shear modulus' is retrieved performing the required compensations (Supplementary Text 2). Furthermore, fittings from first two third-order models can be applied to the data set by selecting the respective initial conditions. Analysis of other calibration experiments such as the Strokes-drag force measurements, creep compliance measurements, and simulations was done on

personalized Matlab and Python scripts.

Methods-only References

[83] Català, F., Marsà, F., Montes-Usategui, M., Farré, A., Martín-Badosa, E., Influence of experimental parameters on the laser heating of an optical trap. *Scientific Reports* **7**, 1–9 (2017).

[84] Schaffer, E., Norrelykke, S. F., Howard, J., Surface Forces and Drag Coefficients of Microspheres near a Plane Surface Measured with Optical Tweezers. *Langmuir* **23**, 3654–3665 (2007).

[85] Brandt, M., Gerke, V., Betz, T., Human endothelial cells display a rapid tensional stress increase in response to tumor necrosis factor-α. *PLoS ONE* **17**, 1–24 (2022).

[86] Behrndt, M., et al., Forces driving epithelial spreading in zebrafish gastrulation. *Science* **338**, 257–260 (2012).

[87] Kimmel, C. B., Ballard, W. W., Kimmel, S. R., Ullmann, B., Schilling, T. F., Stages of embryonic development of the zebrafish. *Dev Dyn* **203**, 253–310 (1995).

[88] Schubert, R., et al., Assay for characterizing the recovery of vertebrate cells for adhesion measurements by single-cell force spectroscopy. *FEBS Letters* **588**, 3639–3648 (2014).

[89] Krieg, M., et al., Tensile forces govern germ-layer organization in zebrafish. *Nature Cell Biology* **10**, 429–436 (2008).

[90] Stiernagle, T., Maintenance of C. elegans. *WormBook : the online review of C. elegans biology* 1–11 (2006).

[91] Porta-de-la Riva, M., Fontrodona, L., Villanueva, A., Cerón, J., Basic Caenorhabditis elegans methods: Synchronization and observation. *Journal of Visualized Experiments* e4019 (2012).

[92] Arribere, J. a., et al., Efficient Marker-Free Recovery of Custom Genetic Modifications with CRISPR/Cas9 in Caenorhabditis elegans. *Genetics* **198**, 837–846 (2014).

[93] Kim, H., et al., A Co-CRISPR strategy for efficient genome editing in Caenorhabditis elegans. *Genetics* **197**, 1069–1080 (2014).

[94] Paix, A., Folkmann, A., Seydoux, G., Precision genome editing using CRISPR-Cas9 and linear repair templates in C. elegans. *Methods* **121-122**, 86–93 (2017).

[95] Malaiwong, N., Porta-de-la Riva, M., Krieg, M., FLInt: single shot safe harbor transgene integration via Fluorescent Landmark Interference. *G3 (Bethesda, Md.)* **13**, jkad041 (2023).

[96] Stemmer, M., Thumberger, T., Del Sol Keyer, M., Wittbrodt, J., Mateo, J. L., CCTop: An intuitive, flexible and reliable CRISPR/Cas9 target prediction tool. *PLoS ONE* **10**, 1–11 (2015).

[97] Goudeau, J., et al., Split-wrmScarlet and split-sfGFP: tools for faster, easier fluorescent labeling of endogenous proteins in Caenorhabditis elegans. *Genetics* **217** (2021).

[98] López-Quesada, C., et al., Artificially-induced organelles are optimal targets for optical trapping experiments in living cells. *Biomedical Optics Express* **5**, 1993 (2014).

[99] Schultz, R. D., Gumienny, T. L., Visualization of Caenorhabditis Elegans Cuticle Structures Using the Lipophilic Vital Dye, DiI. *Journal of Visualized Experiments* 1–6 (2012).

[100] Alberti, S., et al., A User's Guide for Phase Separation Assays with Purified Proteins. *Journal of Molecular Biology* **430**, 4806–4820 (2018).